Bioactive glass (type 45S5) nanoparticles: in vitro reactivity on nanoscale and biocompatibility

Mačković, M ; Hoppe, A ; Detsch, R ; Mohn, D ; Stark, W J ; Spiecker, E ; Boccaccini, A R

DOI: https://doi.org/10.1007/s11051-012-0966-6

Bioactive glass (type 45S5) nanoparticles: In vitro reactivity on nanoscale and biocompatibility

M. Mačković[1,2,¥], A. Hoppe[1¥], R. Detsch[1], D. Mohn[3,4], W.J. Stark[3], E. Spiecker[1,2,*] and A.R. Boccaccini[1,*]

¥ These two authors share the first authorship

[1]Institute of Biomaterials, Department of Materials Science and Engineering, University of Erlangen-Nürnberg, Cauerstr. 6, 91058 Erlangen, Germany

[2]Center for Nanoanalysis and Electron Microscopy (CENEM), Department of Materials Science and Engineering, University of Erlangen- Nürnberg, Cauerstr. 6, 91058 Erlangen, Germany

[3]Institute for Chemical and Bioengineering, ETH Zurich, Wolfgang-Pauli-Str. 10, 8093 Zurich, Switzerland

[4]Department of Preventive Dentistry, Periodontology, and Cardiology, University of Zurich Center of Dental Medicine, Plattenstr. 11, 8032 Zurich, Switzerland

* Corresponding authors:

Aldo R. Boccaccini (Aldo.Boccaccini@ww.uni-erlangen.de; Phone: +49-9131-85-28601; Fax: +49-9131-85-28602) and

Erdmann Spiecker (Erdmann.Spiecker@ww.uni-erlangen.de; Phone: +49-9131-85-28603; Fax: +49-9131-85-28602)

Keywords: Nanoparticles, bioactive glass, TEM, hydroxyapatite, osteoblast

Abstract

Bioactive glasses represent important biomaterials being investigated for the repair and reconstruction of diseased bone tissues, since they exhibit outstanding bonding properties to human bone. In the present study bioactive glass (type 45S5) nanoparticles (nBG) with a mean particle size in the range of 20-60 nm, synthesized by flame spray synthesis, are investigated in relation to in vitro bioreactivity in simulated body fluid (SBF) and response to osteoblast cells. The structure and kinetics of hydroxyapatite formation in SBF were investigated using transmission electron microscopy (TEM), X-ray diffraction (XRD) and Fourier-Transform Infrared Spectroscopy (FT-IR) revealing a very rapid transformation (after 1d) of nBG to nanocrystalline bone-like carbonated HAp. Additionally, calcite is formed after 1d of SBF immersion due to the high surface reactivity of the nBG particles. In the initial state nBG particles were found to exhibit chain-like porous agglomerates of amorphous nature which are transformed upon immersion in SBF into compact agglomerates covered by hydroxyapatite with a reduced size of the primary nanoparticles. In vitro studies revealed high cytocompatibility of nBG with human osteoblast cells, indicated through high lactatedehydrogenase (LDH) and mitochondrial activity as well as alkaline phosphatase activity. Hence, this study contributes to the understanding of the structure and bioactivity of bioactive glass (type 45S5) nanoparticles, providing insights to the phenomena occurring at the nanoscale after immersion in SBF. The results are relevant in relation to the understanding of the nanoparticles' bioreactivity required for applications in bone tissue engineering.

1. Introduction

Due to their attractive biological properties and appropriate mechanical performance bioactive glasses, such as standard 45S5 Bioglass® (BG) is being widely considered in the fields of bone tissue engineering (Hench et al. 2004), applied as bone graft materials for small bone defects as bioactive coatings for orthopedic implants (Gabbi et al. 1995) and as filler particles in biopolymer composites (Rezwan et al. 2006; Boccaccini et al. 2005). Bioactive materials must possess controlled degradation behavior and kinetics that should synchronize with the sequence of cellular changes occurring during new tissue formation (Hench et al. 2004; Gabbi et al. 1995; Rezwan et al. 2006). In the field of bone engineering, bioactivity is defined as the ability of the material to bond to bone tissue via the formation of a bone-like hydroxyapatite (HAp) layer on its surface (Hench 1998; Kokubo et al. 1990). Kokubo (1991) proposed that the essential requirement for an artificial material to bond to living bone is the formation of bonelike apatite on its surface when it is implanted in the living body and that this in vivo formation of HAp can be reproduced in a simulated body fluid (SBF) with ion concentrations nearly equal to those of human blood plasma (Kokubo et al. 1990). Despite some critical considerations on the validity of the SBF technique, this method continuous to be applied to assess the bioactivity behavior of biomaterials (Bohner and Lemaitre 2009). Detailed analysis of the surface apatite formed in SBF solution has been investigated by means of several methods such as transmission electron microscopy (TEM), scanning electron microscopy (SEM), thin-film X-ray diffraction (XRD) and Fourier-Transform Infrared Spectroscopy (FTIR) and it has been shown that it is similar to bone material, both in its structure and in its composition (Kokubo et al. 1990; Ohtsuki et al. 1995). The rate of HAp formation on bioactive glass surfaces depends amongst other factors on the morphology and structure of the material. The recently developed nanosized bioactive glass particles (Brunner et al. 2006) represent an attractive alternative to glass particles in the micrometer range for hard tissue regeneration, since their small particle size makes them ideal for injectable carrier for

effective introduction into bone defects. Furthermore, their larger surface area should lead to increased interface effects, accelerate their interaction with tissue and improve mechanical properties when used in compounds (Boccaccini et al. 2010) and, thus, contribute to an improved bioactivity, compared to standard μm-sized particles (Brunner et al. 2006; Loher 2006) making nanoscaled bioactive glass particles very promising for biomedical applications. For example, nanoscaled bioactive glass particles (n-BG) have been shown to exhibit higher bioactivity, enhanced protein adsorption and to provide significant higher stiffness effect when used as filler in P(3HB) matrices (Misra et al. 2008). Moreover, nanoscaled sol-gel derived S70 bioactive glass particles containing nano-pores have been shown to enhance the interaction with fibrinogen which depends on the nano-sized porosity and the dissolution kinetics of the bioactive glass (Lin et al. 2011). Nanoscaled 45S5 bioactive glass particles (same as used in this study) were also reported to exhibit antibacterial properties (Waltimo et al. 2007) and to have potential for dentin remineralisation (Vollenweider et al. 2007; Curtis et al. 2010) when applied to demineralised dentin matrix. Despite these obvious advantages and great potential of nano and sub-micron sized bioactive glass particles for tissue engineering applications, there are several concerns about bioactive glass (and mixed inorganic nanoparticles in general) being applied in the human body, which could potentially cause tissue damage or cytotoxicity. Especially for bioactive glasses, which are dissolved in physiological medium creating even smaller particles being released in tissue or cell surroundings, only little is known about the potential risks for biomedical applications (Nel et al. 2009). Labbaf et al. (2011) investigated sub-micron bioactive glass particles (SMBGs) of composition, 85 mol% SiO_2 and 15 mol% CaO, synthesized by the sol-gel process. They observed bioactivity by the formation of hydroxyapatite after immersion for 5 days in SBF solution and revealed that these particles did not cause any significant cytotoxicity on hMSCs (Human mesenchymal stem cells) until 4 days of culture. It was shown, however, that the particles caused significant reduction in cell viability after 7 days of

cell culture. The biological properties of nanosized inorganic bone substitute materials cytocompatibility and osteoconductivity are being extensively investigated. It is well-known that nanoscaled materials may exhibit very different physical, chemical and biological properties compared to µ-sized materials of the same composition. However, the mechanisms of nanosized particle-cell interactions are still not fully understood (Nel et al. 2009). The plasma membrane of cells is a selectively permeable membrane for small and nonpolar molecules such as O_2 and CO_2, which can diffuse across the lipid bilayer easily. Polar molecules such as ions and larger particles (nanosized) are unable to pass the plasma membrane on their own. In the case of particles, cells can uptake (Limbach et al. 2005) or enclose them in membrane vesicles by the so called endocytosis process (Sahay et al. 2010). However, in many cases, particles do not interact with cell membranes. Adsorption of proteins on the nanosized particle surface can lead to agglomeration, which prevents its ability to the endocytosis process. Furthermore, nonspecific interactions can also lead to bind nanosized particles to the extracellular matrix (ECM). In addition, alterations of the ECM caused by nanosized particles will also lead in a dramatic change of cell behavior. The interaction of nanosized materials and cells is influenced by shape and size as well as crystallinity and material composition of the nanoparticles (Nel et al. 2009). Therefore, examining the cytotoxic potential of nanoparticles and its correlation with particle characteristics is required for assessing the real applicability of the nanoparticles especially in the field of bone regeneration. In a previous work it has been shown that bioactive glass nanopowders produced by flame spray synthesis exhibit HAp formation after 5 days of immersion in SBF as observed by means of Raman spectroscopy, SEM and XRD analysis (Brunner et al. 2006). In the present study we provide a systematic and more comprehensive investigation of the structure and bioreactivity kinetics occurring on the nanoscale during immersion of the nanosized 45S5 bioactive glass particles in SBF for different time points. Furthermore, cell culture tests are carried out in order to assess the cytocompatibility of these

glass particles. The overall aim of this paper is, thus, to provide the understanding of the structure and bioactivity occurring on the nanoscale of bioactive glass (type 45S5) nanoparticles and to assess the osteoblast cell response of these particles to their future applications in bone tissue engineering, dentistry, wound healing and guided nerve regeneration.

2. Experimental section

2.1. Materials

Nanoscaled bioactive glass particles (type 45S5), nBG, were synthesized by means of flame spray synthesis, as described elsewhere (Brunner et al. 2006). Briefly, the synthesis occurred by combining and mixing the corresponding liquid metal precursors and feeding the mixture into a flame reactor. The nanopowder was collected on a filter mounted above the flame. The specific surface area of the obtained nBG is 60 to 80 $m^2 g^{-1}$. As reference material melt-derived 45S5 micron sized bioactive glass (μBG) with a mean particle size of D_{50}= 10 μm was used. For glass fabrication analytical grades of SiO_2, Ca_3PO_4, $NaCO_3$ and $CaCO_3$ were mixed and melted in platinum crucible at 1450 °C. The fritted glass was dried and milled down to the required particle size (10 μm) using a planetary mill with zirconia jar and zirconia milling beads. The properties of the glass powders used are given in Table 1. The chemical composition (see Table 2) of the glass samples used was verified by laser ablation inductively coupled plasma mass spectroscopy (LA-ICP-MS).

2.2 In vitro bioactivity testing in simulated body fluid (SBF)

The in vitro bioactivity of the samples (nBG and μBG) was tested by immersing the glass powders in simulated body fluid (SBF). SBF solution was prepared according to Kokubo et al. (2006). The pH value of SBF was adjusted to 7.4 at 37.0 °C, by using Tris(hydroxymethyl) amino methane and hydrochloric acid. The ionic concentrations of the inorganic components are given in Table 3. 75 mg of nBG powder were immersed in 50 ml SBF at 37 °C for 4h, 8h,

1d, 3d and 7d, respectively. The samples were stirred at 120 rpm using an orbital shaker (KS 4000i control, IKA, Staufen, Germany). After SBF soaking the nBG powder was filtered, gently rinsed with distilled water and dehydrated with acetone. The samples were dried at 60 °C for 24h before characterization.

2.3 Cell culture tests

Cell culture and sample preparation

To evaluate the cell behaviour of nBG compared with µBG, MG-63 osteoblast-like cells (Sigma-Aldrich, Germany) were used. This human osteosarcoma cell line was cultured at 37 °C in a humidified atmosphere of 95 % air and 5 % CO_2, in DMEM (Dulbecco's modified Eagle's medium, Gibco, Germany) containing 10 vol.% fetal bovine serum (FBS, Sigma-Aldrich, Germany) and 1 vol.% penicillin/streptomycin (Sigma-Aldrich, Germany). Cells were grown for 48 hours to confluence in 75 cm^2 culture flasks (Nunc, Denmark), washed with phosphate buffered saline (PBS) before harvested using Trypsin/EDTA (Sigma, Germany), counted by a hemocytometer (Roth, Germany) and diluted to a final concentration of 100.000 cells ml^{-1}. Before cell seeding, the µBG and nBG particles were dispersed in 70% ethanol and sonicated for 30-60 min. Then, bioactive glass (BG) containing ethanol suspension was transferred into 48 well plates and ethanol was completely evaporated in a drying chamber. MG-63 cells were exposed to varying concentrations (0.1, 1, 10, 100 and 200 µg ml^{-1}) of BG particles present in final volume of 600 µl culture media for 48 hours. The *in vitro* analysis of BG was compared to ZnO particles (Oxiznic Agalsa, Spain) with the same concentrations as used for BG. ZnO is the positive control for cytotoxicity in this investigation. Therefore, LC_{50} value (lethal concentration of the used particles where the activity of the cells is reduced to 50%) was calculated. During cell incubation and after 48h of incubation cell distribution and morphology in contact with BG and ZnO were evaluated using phase contrast light microscopy (LM, Nikon Eclipse TE 2000-U, Japan).

LDH-activity

Lactate dehydrogenase (LDH-) activity gives a measurement of the amount of attached cells on the BG. LDH reduces NAD^+, which catalyses the conversion of tetrazolium to a coloured formazan derivative. A commercially available LDH-activity quantification kit (TOX7, Sigma-Aldrich) was used to quantify cell proliferation by enzyme activity in cell lysate. MG-63 cells cultured in 48-well plates were washed with PBS and lysed with lysis buffer for 10 minutes (1 ml/well). The lysate solutions were centrifuged by 250 g and 100 µl from the supernatant solutions were transferred to a 98-well plate. 30 µl of Master-mix were added to each well containing equal amounts of: substrate solution, dye solution and cofactor solution for LDH assay. The plates were left for 30 minutes in the dark and the reaction was stopped with 40 µl HCl 1 N per well. The dye was measured using a spectrophotometer (SPECORD 40 BU, analytikjena, Germany) at 490 nm.

Mitochondrial activity

For assessing the influence of different BG and ZnO concentrations on the viability of MG-63 cells after 2 days of culture, a WST-8 assay (Sigma-Aldrich) was used. After a cultivation period of 48 hours, the mitochondrial activity of MG-63cells was measured by the conversion of tetrazolium (WST-8, Sigma) to formazan by mitochondrial enzymes. Culture media was removed from the 48-well wells plates and the cells were washed with PBS. After addition of 100 µl of solution containing 99 µl culture medium and 1 µl WST-8 in each well, the plates were incubated for 1 h. Afterwards the supernatant of all samples was transferred and centrifuged by 250 g. Subsequently, the solution was given in a 98-well plates (50 µl in each well) to measure the absorbance at 450 nm and 650 nm with an ELISA-Reader (Perkin Elmer, Multilabel Reader Enspire 2300, Germany).

Vybrant™ cell-labeling

The samples were prepared for confocal scanning laser microscopy (CSLM, Leica TCS SP5 II, Germany) to analyse cell morphology and distribution. To analyse the adherent growth of

cells on the bioactive glass samples, Vybrant™ cell-labeling solution (Molecular Probes, The Netherlands) was used. After 48 hours of incubation, cell culture medium was removed and staining solution (5 µl dye labelling solution to 1 ml of growth medium) was added and incubated for 15 min. Afterwards the solution was removed, the samples were washed with PBS (phosphate buffered saline, Gibco) and cells on the BG samples were fixed by 3.7 vol.% paraformaldehyde.

Specific Alkaline phosphatase (ALP) activity

ALP is a membrane-bound metalloenzyme which catalyzes the hydrolysis of phosphomonoesters at an alkaline pH. For determining the osteoblastic activity of the MG-63, ALP was analysed by measuring the specific enzyme activity after 48 hours of incubation with BG. After lysing the cells with a cell lysis buffer containing 20 mM TRIS buffered solution (Merck) with 0.1 wt% Triton X-100 (Sigma, Germany), containing 1 mM $MgCl_2$ (Merck) and 0.1 mM $ZnCl_2$ (Merck), the absorption was measured at 405 nm using a spectrometer after 90 min of incubation. The specific activity was then calculated with respect to the protein concentration of the cell lysates. Therefore, the protein content of the cell lysates was determined using a commercial kit based on Bradford assay (Sigma).

Statistical analysis

Each experiment was repeated four times. The results are presented as average and standard deviation of four replicates with the values. Samples with 0 µg ml^{-1} BG and ZnO were set as 100%. The differences in analysis parameters between the BG concentrations were evaluated by one-way analysis of variance (ANOVA). The level of the statistical significance was defined at $p < 0.05$ (Origin 8.1G, OriginLab Corporations, USA).

2.4 Characterisation techniques

Transmission electron microscopy (TEM) was carried out using a Phillips CM30 TWIN/STEM, equipped with an energy dispersive X-ray (EDX) spectroscopy detector for analytical analyses. Further TEM investigations are performed using a Titan^3 80-300

equipped with a field-emission gun, an image-side aberration corrector and also an EDX detector. TEM images were acquired using charged coupled device (CCD) cameras, having an image size of 1024 x 1024 pixels at the CM30 and 2048 x 2048 pixels at the Titan^3, respectively. Both microscopes were operated at 300 kV acceleration voltage. Furthermore, all TEM analyses were performed using a Gatan Model 636-DH double tilt liquid nitrogen (LN_2) cooled specimen holder, which enables TEM investigations at -170°C specimen temperature and prevents damage caused by the electron beam. For TEM investigations, all samples were dispersed in a H_2O/Ethanol solution and deposited on lacey carbon film coated gold grids.

Fourier-Transform Infrared Spectroscopy (FT-IR) was used to identify the formation of reaction phases during the immersion of the samples in SBF. FT-IR spectra of the glass powders prior and after soaking in SBF solution were collected in transmission (Impact 420, Nicolet Instr., Walthem, MA, US) in the frequency range 400-4000 cm^{-1} using the KBr method. For KBr pellets a sample/KBr ratio of 1/300 was used. The spectra were collected accumulating 64 scans with a resolution of 4 cm^{-1}. The spectra were base-line corrected and normalized to the main silicate glass peak at ~ 1050 cm^{-1} in order to compare the intensities of the bands within one sample.

X-ray diffraction (XRD) analysis was used to investigate the structure and phase composition present in the bioactive glass samples after immersion in SBF. The XRD data were collected with a Bruker D8 Advance powder diffractometer with a graphite secondary monochromator using Cu K_α radiation (λ = 0.15406 nm). The XRD patterns were acquired with a step width of 0.014 and 1s time per step. The samples were measured over a 2θ range from 20° to 80°. As reference, XRD spectra of the as-prepared powders were recorded.

3. Results

3.1 In vitro bioactivity

The kinetics of hydroxyapatite formation on nanoscaled glass particles were monitored by FT-IR measurements and compared to micron sized 45S5 powder. The major bands appearing in the IR-spectra are summarised in Table 4. Fig. 1 a) shows the FT-IR spectra of the micron-sized glass (μBG) samples as-received and after immersion in SBF for 4h, 8h, 24h, 3d and 7d. For the as-prepared sample without any treatment in SBF the bands at ~500 cm^{-1} and ~1030 cm^{-1} can be assigned to ν_{sym}(Si-O-Si) and ν_{asym}(Si-O-Si) bands of the SiO_4 tetrahedra, respectively (Cerruti et al. 2005). Due to the presence of Ca^{2+} and Na^{+} cations in the glass network the ν_{sym}(Si-O-Si) band is shifted to 500 cm^{-1} compared to pure silica (ν_{sym}(Si-O-Si) at 450) (Bunker et al. 1998). The band at ~930 cm^{-1} can be attributed to the SiO_{NBO} (non-bonding oxygen, NBO) which is formed through the presence of the glass network modifier, creating Si-O groups (Bunker et al. 1998). At ~1450 cm^{-1} a broad peak is seen which can be assigned to the $\nu_3(CO_3^{2-})$ band of carbonates adsorbed on surfaces (Du et al. 2010). After the initial stage of SBF immersion (4h) this single peak is split into two separate bands, but with lower intensity at 1430 cm^{-1} and 1500 cm^{-1}, respectively. With increasing immersion time in SBF the intensity of the SiO_{NBO} band is decreasing becoming a weak shoulder after 4h of SBF immersion which is due to the ion exchange in the glass network and leaching of Na^{+} and Ca^{2+} ions. Also the ν_{sym}(Si-O-Si) band is shifted to 460 cm^{-1} as observed for pure silica (Bunker et al. 1998). At ~ 600 cm^{-1} a broad peak is observed which can be attributed to formation of an amorphous calcium phosphate (ACP) (Hench 1998; Cerruti et al. 2005).

After 3d of soaking in SBF the SiO_{NBO} intensity slightly increases again, whereby the overall position of this peak is shifted from 930 cm^{-1} towards 960 cm^{-1}. This shift is possibly related to the higher frequency of SiO absorption as a result of lower content of the NBOs (Cerruti et al. 2005). For all stages of the SBF immersion an additional band at ~1210 cm^{-1} is detected which is assigned to ν(Si-O-Si) mode. After 3d immersion the δ(Si-O-Si) band appears at

~800 cm^{-1} which is related to the formation of highly disordered 3D silica structure (Cerruti et al. 2005). After 3 d of immersion in SBF bending modes of ν_4(P-O-P) bond from the PO_4^{3-} group at ~570 cm^{-1} and ~600 cm^{-1} are detected. The ν_2(P-O-P) bending mode is also observed at ~471 cm^{-1} which, however, is overlapped with the ν_{sym}(Si-O-Si) band of the glass network (Koutsopoulos 2002). An additional band at 871 cm^{-1} appearing after 3d of SBF immersion can be assigned to $\nu_2(CO_3^2)$. Moreover, the intensity of the $\nu_2(CO_3^2)$ bands at 1430 cm^{-1} and 1500 cm^{-1} increased along with increasing SBF immersion time. Fig. 1 b) shows the FT-IR spectra for the nanoscaled bioactive glass particles prior and after 4h, 8h, 24h, 3d and 7d immersion in SBF. Basically, the spectra exhibit similar characteristic bands as observed for µBG. However, the relative intensity and time point of appearance of the absorption bands can differ, as documented in Table 4. In the as-prepared state the nBG shows a significantly higher intensity of the carbonate signal at 1450 cm^{-1}. Additionally the carbonate band at 871 cm^{-1} appears also in the initial state of the sample. After 4h in SBF the intensity of $\nu_2(CO_3^2)$ band drops, but is increasing again with increasing immersion time. Furthermore, the bands at 800 cm^{-1} and at ~600 cm^{-1} appear already after 4h compared to µBG. After 3d a weak additional peak at 712 cm^{-1} is observed which can be attributed to calcite (Bosch et al. 2002). For both glasses investigated adsorbed coordinated water molecules were detected on the surface (at ~ 1630 cm^{1-}).

Fig. 2 a) shows the XRD spectra of the as-prepared µBG and after immersion for 1, 3 and 7 days in SBF. The absence of reflections in the XRD pattern of the as-prepared sample confirms the formation of the amorphous structure of the bioactive glass powder. After 1d no formation of any crystalline phase is observed, whereas after 3d and 7d the formation of carbonated hydroxyapatite, CHAp $Ca_{10}(PO_4)_6(CO_3)_{0.5}(OH)$, (ICDD PDF 2 01-089-4405) is detected. The main characteristic peaks of CHA are at $2\Theta=26°$ (002) and $2\Theta=31.5°$ (112).

Fig. 2 b) shows the XRD spectra of the nBG after 1, 3 and 7 days in SBF. The amorphous characteristics of the flame-synthesized nanoscaled bioactive glass was confirmed. After 1

day a weak signal is detected at 2Θ=31.5° suggesting the formation of CHA. After 3d and 7d of immersion formation of CHAp can be clearly seen from the pronounced signals at 2Θ=26° and 2Θ=31.5°. Aside from CHAp calcite (ICDD PDF2 01-0713695) is also formed after 3d and 7d of immersion in SBF. Using the Scherrer equation the crystallite size D_{hkl} perpendicular to (*hkl*) lattice planes can be calculated as follows (Danilchenko et al. 2002):

$$D_{hkl} = \frac{K\lambda}{FWHM_{hkl}\cos\theta} \quad (1)$$

Here K, Θ, λ and $FWHM_{hkl}$ are the shape factor, diffraction angle, the wavelength of the x-rays and the full width at half maximum of the *(hkl)* peak, respectively. For hydroxyapatite and for calcite formed after 7 days in SBF a crystallite size of D_{112}= 5.5 nm and D_{104}=91.4 nm were calculated, respectively.

Fig. 3 a) and b) show bright-field TEM images of the as-prepared nBG. The particles exhibit chain-like agglomerates and are structurally amorphous, as confirmed by SAED (inset in Fig. 3 a)). TEM images show that the primary nanosized glass particles are fused together and irregularly shaped, thus making it difficult to make precise conclusions about their size. However, the particle size was estimated to be 20 - 60 nm in diameter. Fig. 3 c) – f) shows bright- and dark-field TEM images and SAED pattern of nBG after immersion for 1 day in SBF. Generally, formation of nanocrystalline HAp and co-precipitation of nanocrystalline and coarse calcite is observed, as confirmed by the SAED (insets in Fig. 3 c), d) and e)). The HAp found here has a hexagonal crystal structure with $P6_3/m$ space group symmetry and lattice parameters $a = b$ = 0.94 nm, c = 0.69 nm (ICSD_150309). The observed calcite also has a hexagonal crystal structure with $P6_3/m$ space group symmetry and lattice parameters $a = b$ = 0.49 nm, c = 1.71 nm (ICSD_15879). Unreacted nBG is still present after 1 day in SBF. This is evident from the TEM images in Fig. 3 c) and d) showing a network of nanoparticles which exhibit shapes being similar to the ones found in the as-prepared sample. Moreover, after immersion for 1 day in SBF HAp is also found to precipitate completely separated, as shown

in Fig. 3 d) and inset in Fig. 3 d). Both DP (insets in Fig. 3 c) and d)) appear blurred, which can be attributed to the signal coming from amorphous nBG still being present unreacted. At last, after immersion for 1 day in SBF calcite crystals are also found to precipitate separately. The DP (inset in Fig. 3 e)) was tilted into the [10-12] zone axis and indicates that this calcite is single-crystalline. Dark-field imaging for the (-12-10) reflection (see Fig. 3 f)) reveals the location of the calcite crystals. After immersion of nBG for 7 days in SBF formation of calcite and HAp was observed. Fig. 4 a) shows a bright-field TEM image of calcite crystals coexisting besides unreacted amorphous nBG. SAED (insets i) and ii) in Fig. 4 a)) confirms the hexagonal crystal structure of calcite. On the one hand the SAED pattern (inset i) in Fig. 4 a)) indicates the presence of single-crystalline calcite (sharp diffraction dots in the pattern), where the calcite crystals reach sizes of up to ~ 800 nm in diameter and exhibit irregular morphologies. On the other hand, the same SAED pattern shows additional rings besides the sharp dots, which indicates the presence of calcite nanocrystals. Thus, a mixture of calcite nanocrystals and single crystals is present. Fig. 4 b) shows that the calcite nanocrystals surround the bigger calcite crystals, which is evident from the diffraction-contrast of crystalline particles being in Bragg-condition. In order to locate the calcite crystals, more accurate dark-field TEM imaging was performed within the area marked with the bigger dotted circle in Fig. 4 a). The corresponding dark-field images of the (113) and (104) reflections are shown in Fig. 4 c) and d). It is worth to mention that during dark-field imaging of these two reflections the sharp dots and the corresponding parts of the ring pattern are both contributing to the dark-field images (due to the limiting size of the objective aperture), since the sharp dots are located exactly on the corresponding reflections of the ring pattern. However, these images additionally support that the coarse calcite crystals are surrounded by calcite nanocrystals. At last, for the same sample after immersion for 7 days in SBF, completely isolated more compact agglomerates (compared to the as-prepared nBG) are observed, as shown exemplarily in Fig. 4 e) and f). The agglomerates contain a significant

amount of HAp, which is confirmed by SAED (inset in Fig. 4 e)). As shown in Fig. 4 f) the agglomerates consist of irregularly shaped but also spherical and nearly-spherical particles, which reach sizes of 5 - 25 nm in diameter. The transformation of the nBG into HAp and calcite is also confirmed by TEM EDX spectroscopy analysis, as shown in the inset of Fig. 4 b). The EDX spectrum of the as-fabricated nBG shows the typical chemical composition of this glass (see inset in Fig. 3 b)). The Ca/P ratio changes from 6.20 for the as-prepared nBG to 12.06 after immersion in SBF for 7 days. Moreover, a significant decrease of the sodium concentration is observed.

3.2 Results of the *in vitro* investigation

Fig. 5 shows the LDH-activity of MG-63 cells cultured on µBG, nBG and ZnO in the range of 0-200 µg ml^{-1} over 48 h. ZnO particles induced a reduction in cell viability at higher concentrations. Thus the calculated LC_{50} value for ZnO is approx. 31 µg ml^{-1}. Both µBG and nBG exhibit no reduced LDH-activity even at high concentration of 200 µg ml^{-1}. At the concentrations of 0.1-100 µg ml^{-1} significant higher amount of MG-63cells grew on nBG compared to µBG.The cell viability of MG-63 cells cultured on µBG, nBG and ZnO in the range of 0-200 µg ml^{-1} over 48 h measured by mitochondrial activity is shown in Fig. 6. In case of ZnO there is an optimum concentration of 0.1 µg ml^{-1} for cell viability. The LC_{50} value was determined to be 41 µg ml^{-1}. Again, for µBG and nBG, no reduction in cell viability was found. Comparing the two BG samples, 10 and 100 µg ml^{-1} concentrations of nBG induced a significant higher viability in MG-63 cells. MG-63 cells expressed mainly elongated and polygonal phenotype and an almost dense cell layer in the cell culture dish after 48 h of cultivation. LM-images of the MG-63 cell morphology grown on ZnO, Fig. 7 a), confirmed the LDH- and mitochondrial activity measurements. The cell layer at 0.1 µg ml^{-1} is most dense and cells are most vital, which can be correlated with results in Fig. 6. Furthermore, at the ZnO concentration 10 - 200 µg ml^{-1} reduction of cells can be seen and

changes in the morphology of MG-63 cells are observed, which become round. At the highest concentration, 200 µg ml^{-1} agglomeration of ZnO particles and no cells could be detected.

Morphology analysis of MG-63 cells in contact with different µBG concentrations confirmed also the LDH- and mitochondrial activity measurements. The LM-images in Fig. 7 b) demonstrate no influence of µBG on MG-63 cell morphology. Compared to µBG, the analysis of morphology on nBG showed similar results (Fig. 7 c)). No obvious effect could be detected on cells during the cultivation with nanosized BG particles. However, at the highest concentration of nBG (200 µg ml^{-1}) agglomerates can be even detected by LM. Vybrant™ cell-labeling was used to display the cells at higher magnifications. In Fig. 8 CLSM-images of MG-63 cultured with 200 µg ml^{-1} µBG and 200 µg ml^{-1} nBG and without contact to any BG particles were shown. With or without BG particles cells form their typical elongated and polygonal morphology, including cell-cell contacts. Even at this highest concentration of 200 µg ml^{-1} no influence of BG particles on MG-63 cells could be found. Osteoblastic activity was investigated by means of specific ALP activity (Fig. 9). Measured ALP activity was comparable at all µBG concentrations, indicating a similar degree of osteoblastic activity. In addition, the cultivation of MG-63 cells on nBG induced an increase of specific ALP-activity, which was even significantly higher on concentration of 200 µg ml^{-1}.

4. Discussion

4.1 As-prepared stage

The nBG synthesized by flame spray synthesis was investigated in terms of their *in vitro* bioactivity and cell response. TEM and XRD analysis confirmed the amorphous structure of the as-fabricated nBG since no evidence of a crystalline phase is detected, comparable to an earlier study (Brunner et al. 2006). The nBG investigated in the present work exhibits chain-like agglomerates.

4.2 In vitro reactivity in SBF

The reaction stages in the SBF monitored by FT-IR showed the presence of carbonate species on the μBG as well as nBG particles. For the as-received materials these compounds detected can be attributed to carbonate species adsorbed on the surface. The single peak at ~1460 cm^{-1} indicates the presence of purely ionic carbonate-like structures with high symmetry which are likely adsorbed on the glass surface upon reaction with CO_2 in air (Du et al. 2010; Cerruti and Morterra 2004). Interestingly, the intensity of this band is higher in the nBG sample than in the μBG and additionally the carbonate band at 871 cm^{-1} appears also in the initial state of the nBG sample which is likely due to the higher specific surface of the nanoscaled glass powder resulting in larger quantities of adsorbed species. After contact with liquid medium during the first stage of reaction in SBF, i.e. after 4 h (see Fig. 1 a) and Fig. 1 b)) the single peak at 1460 cm^{-1} is split to a double peak related to asymmetric surface carbonate structures. Since it is known that the BG surface is depleted in Na^+ and enriched with Ca^{2+} ions, through migration of the ionic species from the bulk glass to the surface, the change in CO_3^{2-} symmetry is likely due to formation of calcium coordinated carbonate structures ($Ca^{2+}\cdots CO_3^{2-}$) (Cerruti and Morterra 2004; Cerruti et al. 2005). However, the $\nu_3(CO_3^{2-})$ modes represented as double peak (1420 cm^{-1} and 1480 cm^{-1}) can be also attributed to carbonate ions substituted in apatite lattice (Koutsopoulos 2002). According to XRD analysis of the μBG, HAp formation takes place after 3d immersion in SBF. At the same stage there is a sharp increase of the intensity of the $\nu_3(CO_3^{2-})$ modes and additionally the $\nu_2(CO_3^{2-})$ mode appears, which is related to carbonate ions incorporated in HAp. It is suggested that as soon as HAp forms on the glass particle surface the detected carbonate species are dominated by carbonate ions replacing phosphate groups in the HAp lattice. For the nBG samples it is difficult to distinguish between the different carbonate species from the IR spectra since the $\nu_2(CO_3^{2-})$ band is present for the as-received sample and the reaction of the nanoscaled bioactive glass occurs rapidly making it challenging to detect any changes in the IR bands related to carbonate species. However, we

assume that the mechanism for this transformation is valid as for µBG described above. In the next step a silica gel layer is formed on the bioactive glass surfaces (both nBG and µBG) form through condensation reaction of SiOH groups (Hench 1991):

$$2SiOH \rightarrow Si - O - Si + H_2O \quad (2)$$

Further, an amorphous calcium phosphate layer (ACP) as a precursor phase to hydroxyapatite is formed (Hench 1998; Cerruti et al. 2005; Jones et al. 2001; Dey et al. 2010). For the nBG the in vitro reactivity is enhanced compared to µBG since all stages of reaction in SBF including the silica gel and ACP formations as well as HAp crystallisation occur faster (see Table 4). It is well known that SBF and related physiological media are supersaturated in respect to several calcium phosphate phases (Zhu et al. 2003; Müller and Müller 2006). The thermodynamic driving force ΔG for crystallisation of a solid phase from aqueous solution can be expressed using the supersaturation S according to following equation:

$$\Delta G = -\frac{RT}{n}\ln(S) \quad (3)$$

Here R, T and n are the universal gas constant, temperature and number of ions present in the solution, respectively. The supersaturation of a solution S can be calculated using equation (4) with IP, K_{sp} and n being the ionic product activity, the solubility product and the number of ions of the formula, respectively (Nielsen 1984):

$$S = \sqrt[n]{\left(\frac{IP}{K_{sp}}\right)} \quad (4)$$

The supersaturation of a stoichiometric hydroxyapatite (HA, $Ca_{10}(PO_4)_6(OH)_2$), an A-type carbonated hydroxyapatite (A-CHA, $Ca_{10}(PO_4)_6(CO_3)_{0,5}(OH)$), a B-type (B-CHA, $Ca_9(HPO_4)_6(PO_4)_5(CO_3)_{0,5}(OH)$) carbonated apatite and calcite ($CaCO_3$) were calculated according to the equations 5-8 (Müller and Müller 2006):

$$IP_{HA} = [Ca^{2+}]^{10}[PO_4^{3-}]^6[OH^-]^2 {y_1}^2 {y_2}^{10} y_3^6 \quad (5)$$

$$IP_{A-CHA} = [Ca^{2+}]^{10}[CO_3^{2-}]^{0.5}[PO_4^{3-}]^6[OH^-] y_1 {y_2}^{10.5} y_3^6 \quad (6)$$

$$IP_{B-CHA} = [Ca^{2+}]^{10}[HPO_4^{2-}]^{0.5}[CO_3^{2-}]^{0.5}[PO_4^{3-}]^5[OH^-] y_1 {y_2}^{10.5} y_3^5 \quad (7)$$

$$IP_{Calcite} = [Ca^{2+}][CO_3^{2-}]y_2^2 \quad (8)$$

The activity coefficient y_z of an ion with the valence z were calculated using a modified Debey-Hückel equation as proposed by Davis and Shedlovsky (1964):

$$-logy_z = 0.515z^2[\sqrt{I}/(1+\sqrt{I}) - 0.3I \quad (9)$$

Here I is the total ionic strength of the solution and is given by:

$$I = 0.5\sum z_i^2 c_i \quad (10)$$

with z_i and c_i being the charge and the concentration of the i ion, respectively.

The CO_3^{2-} and the PO_4^{3-} concentration were calculated from the ion concentrations given in Table 1 and from the equilibrium constants for the reactions (11) and (12) (Müller and Müller 2006):

$$HCO_3^- + OH^- \leftrightarrow CO_3^{2-} + H_2O \;\; pK = 10.25 \quad (11)$$

$$HPO_4^{2-} \leftrightarrow PO_4^{3-} + H^+ \;\; pK = 12.19 \quad (12)$$

The *IP* and the degree of supersaturation for the phases mentioned above are given in Table 5. For the precipitation of any solid phase to occur the free Gibbs energy ΔG must be <0 which requires S >1. The SBF is supersaturated for stoichiometric hydroxyapatite as well as for carbonated apatites. Moreover, the highest supersaturation is obtained for B-type carbonated apatite, whereby the carbonate ions are incorporated into the apatite lattice by substituting PO_4^{3-} ions (Elliot 1994). Even though the difference in supersaturation between A and B-type apatite is insignificant, the formation of B-type carbonate is thermodynamically favored for precipitation in the SBF used. It has been previously shown that B-type substitution is the dominating mechanism for carbonated apatites especially for SBF solution with lower HCO_3^- content (Müller and Müller 2006; Antonakos et al. 2007). The FT-IR analysis also confirms B-type substitution since the characteristic $\nu_3(CO_3^{2-})$ band at 1450 cm^{-1} for A-type substituted apatite was not observed in the IR-spectra (Koutsopoulos 2002). Moreover, the nanosized characteristics of the CHAp observed by XRD and TEM analyses are typical for biomimetic

hydroxyapatite formed in physiological media (Müller and Müller 2006; Pasteris et al. 2004). TEM investigations revealed nanocrystalline HAp being present within compact agglomerates after immersion for 1 and 7 days in SBF, also coexisting with unreacted nBG. Furthermore, the reduction of the size of the primary bioactive glass nanoparticles is observed after immersion in SBF solution, which indicates the dissolution of nBG and distortion of the chain-like network of the nBG, as discussed above.

Labbaf et al. (2011) investigated submicron spherical bioactive glass particles with the composition 85 mol% SiO_2 and 15 mol% CaO by means of TEM. The particles were produced by the sol-gel process with a mean particle diameter of 250 nm. They found formation of HAp after 5 days immersion in SBF. Hereby, the authors also proposed significant dissolution of the bioactive glass particles and formation of nanoscaled HAp. However, it is difficult to directly compare our study with this work, due to the noted differences in particle size and composition. For instance, in our case the formation of HAp is already observed after 1 day of immersion in SBF by means of TEM, which supports the fact that the reduced particle size of the present nBG compared to the particles investigated by Labbaf et al. (2011) and thus the increased specific surface area significantly increases the potential of the material to form HAp. The high reactivity of nanoparticles confirmed through the very fast formation of CHAp might be also affected by the non uniform structure, morphology and relatively high porosity of the as-prepared nBG, observed by TEM (see Fig. 3 a) and b)). Tilocca (2011) showed in molecular dynamic simulations of Bioglass® nanoparticles that the Na^+/Ca^{2+} ratio is increased for nanoparticles compared to bulk material and that the network connectivity is reduced, indicated through higher Q^1 and lower degree of Q^3 units. Moreover, the mobility of Na^+ ions is increased in the nanoparticles. Since these features are known to accelerate the dissolution behaviour of 45S5 bioactive glass via rapid release of Na^+ ions and exchange with H^+ from the physiological environment they might also explain the enhanced bioactivity of the nBG nanoparticles. An increased reactivity by

reduction of the particle size and thus an increase of the specific surface area has been observed by several researchers for the 45S5-type bioactive glass. Sepulveda et al. (2002) investigated the effect of powder type, particle size (50 – 20 μm (fine size); 90 – 300 μm (medium size); 90 – 710 μm (coarse size)), and type of dissolution medium on the dissolution behaviour of bioactive glasses by means of in vitro testing using melt-derived 45S5-type and sol-gel derived 58S bioactive glass powders. The specific surface area of the fine-sized particles was 2.7 m^2g^{-1}, 0.24 m^2g^{-1} for the medium-sized particles, and 0.15 m^2g^{-1} for the coarse-sized particles, respectively. Amongst other observations, they found that the dissolution and thus the reactivity of the melt-derived 45S5-type bioactive glass is significantly increased for the finer particles ranging from 5 to 20 μm, compared to the more coarse particles ranging from 90 to 710 μm. Although Sepulveda et al. (2002) did not investigate nanometric particles their results support the here presented findings and the fact that a clear trend of higher reactivity can be achieved by reducing the particle size (increasing the specific surface area).

According to Table 5 SBF is undersaturated for calcite precluding the nucleation of calcite in the SBF. Indeed, no calcite formation was found for the micron-sized bioactive glass particles at any stages of reaction in SBF, as proved by FT-IR and XRD analyses. For the nanoscaled bioactive glass particles, however, formation of nanosized and large calcite crystals (≥ 100 nm) was observed by TEM already after 1 day (and 7 days) in SBF, while large calcite crystals are detected by XRD and FT-IR not until 3 days of immersion in SBF. Bioactivity tests in SBF solution revealed the formation of two crystalline phases, calcite and HAp. The high Ca/P peak intensity ratio of ~12, as observed by TEM EDX spectroscopy after immersion for 7 days in SBF, is likely due to the large amounts of calcite precipitations. TEM observations revealed the formation of HAp and calcite already after 1 day immersion in SBF, while XRD and FTIR revealed the formation of HAp starting from day 3 in SBF. This suggests that the amount of HAp and calcite precipitates is not strongly pronounced after

immersion for 1 day in SBF and thus HAp and calcite are not detectable by XRD and FTIR, in those samples, Fig. 1 b) and Fig. 2 b). Moreover, it is worth mentioning that no calcite formation was found on micron-sized glass particles, which might be attributed to the effect of particle size. Jones et al. (2001) observed calcite formation for 45S5 bioactive glass powder particles after 2h of immersion in SBF. It was found that calcite is forming at the expense of HAp for high BG powder concentrations in the SBF solution, likely due to an excessive amount of calcium ions released in the SBF resulting in a higher Ca/P ratio and a pH shift in the SBF solution. This mechanism favoured the precipitation of calcite. Oyane et al. (2003) investigated the formation and growth of $CaCO_3$ clusters in different simulated body fluids. They have shown that SBF solutions depleted in PO_4^{3-} ions and thus high Ca/P ratio can accelerate the precipitation of calcite by increasing the saturation of the solution in respect to calcite. This early HAp formation agrees very well with our TEM results. Moreover, our results indicate that the calcite formation on nBG is likely due to the large surface area of the particles resulting in a high reactivity of the glass surface and enhanced diffusion of Ca ions in the glass network. Mozafari et al. (2010) also observed co-precipitation of calcite beside of hydroxyapatite on mesoporous sol gel derived bioactive glass after 1d of soaking in SBF which was related to the high surface area (~140 m^2 g^{-1}) and nano-porosity of these particles. They proposed that the high surface area allows the high release of calcium (Mozafari et al. 2010). According to the findings in the literature discussed above, the calcite precipitation takes place parallel to the hydroxyapatite formation during the first stages of SBF reactions. Even though the crystalline calcite phase was not detected by FT-IR and XRD until 3 days in SBF, TEM clearly revealed calcite precipitates already formed after 1d in SBF. Thus, we postulate that the calcite nucleation occurs as co-nucleation at very early stages of nBG reaction in SBF. It has been shown previously that the precipitation of calcite is preceded by formation of an amorphous carbonate cluster (ACC) as a precursor phase (Pichon et al. 2008) which is obviously not seen in the XRD spectrum. Moreover, indicated through the large

crystalline size of calcite particle the diffusion driven crystal growth of the calcite phase might need longer time not becoming detectable until 3d of reaction in SBF. Based on our results and the findings in the literature, the following model can be suggested for the reactions occurring at the surface of nBG when exposed to simulated body fluid, as shown in Fig. 10:

- Stage 1 (4h-8h): Dissolution of nBG particles and release of ionic species (e.g. Ca^{2+}, Na^{+}, PO_4^{3-}). The network of primary particles is distorted and the particle size is reduced. Silica layer is formed by condensation of Si-OH groups. Ca^{2+} and PO_4^{3-} ions diffuse through the silica layer forming an amorphous CaP layer (ACP) (Hench 1998). Co-nucleation of an amorphous Calcium-carbonate as precursor phase for calcite occurs.
- Stage 2 (1d): Forming of a 3D silica network and crystallisation of nanocrystalline (5-20 nm) carbonated HAp (type B substitution) and co precipitation of calcite. Three independent structural configurations are formed: i) unreacted nBG with nanocrystalline HAp ii) unreacted nBG with nanocrystalline HA and calcite co-precipitates and iii) unreacted nBG with single-crystalline calcite precipitates.
- Stage 3 (3-7d): Further co-precipitation and growth of larger calcite crystals (≥ 100 nm) at the expense of carbonated hydroxyapatite (CHA). Finally, separated configurations of i) nBG and nanocrystalline HAp and ii) nBG and single-crystalline calcite are present.

As in the present study, for the same nanosized 45S5 bioactive glass particles, Brunner et al. (2006) observed HAp formation by means of Raman spectroscopy and scanning electron microscopy after immersion of nBG pellets for 7 days in SBF. HAp nanocrystals covering the rough surface of bioactive 45S5 glass pressed tablets were observed. However, the specific effect of the nanosized particles was only partially investigated by pressing the glass powder

to dense bulk samples. Thus, the reactions kinetics of the nBG are different since, clearly, the reactivity of single nanoscaled particles is expected to be higher due to the high surface area, as shown in the present work. In the present study, however, HAp formation was investigated by XRD, FTIR and TEM after immersion of the as-prepared nBG powder in SBF for different time points ranging from 4 h to 7 d, monitoring in detail for the first time the reaction kinetics in nBG. Moreover, a formation of calcite was detected, likely due to the high surface area of the particles, which was not considered by Brunner et al. (2006) in the experiments with bulk materials. Unlike bulk materials, the bioactivity of small particles strongly depends on their size and specific surface area (Sepulveda et al. 2002), which is shown in the present work as a fundamental and comparative study.

4.3 Cytocompatibility

In this study ZnO, µBG and nBG particles at the concentrations of 0.1 - 200 µg ml^{-1} were incubated with MG-63 osteoblastic cells over 48 h. All materials were pre-treated in the same way and incubated with the same amount of cells at the same cultivation period. Afterwards cell amount, viability and morphology as well as spec. ALP-activity were analysed. Heng et al. (2011) determined the cytotoxicity effect of ZnO particles and also of Zn^{2+} ions according to cell type, seeding concentration and surface area of the culture well. They showed the importance of the design of the in vitro experiments to measure the cytotoxicity of nanoparticles. Therefore, ZnO particles with a particle size of 0.5-1.5 µm and a specific surface of 6.5 m^2 g^{-1} were used as a reference sample. The detected cytotoxicity of ZnO particles analysed with 100.000 cells over 48 h of incubation ranged in the concentrations between ~ 31 and 41 µg ml^{-1}. These results correspond to the findings of Gann et al. (2010), who showed cytotoxic effects of ZnO particles at concentrations of 31.5 - 62.5 µg ml^{-1}.

Regarding both BG types, no cytotoxic effect was determined even by an increase of particle concentration (see Fig. 6). Although the concentration of BG particles being kept constant, the use of nanosized BG will increase the particle surface to cell area ratio dramatically

(compared to the constant MG-63 cell shape with an area of ~ 950 µm² and a volume 1.3 10^3 µm³) which is expected to lead to a different cell response.

It should be also considered that the nanosized particles undergo sedimentation and agglomeration before cell seeding. Despite this limitation, it is interesting that nBG induced higher activities of MG-63 cells after 48 h of incubation compared to µBG. Even at a higher concentration of 1000 µg ml^{-1} of nBG a remaining cell viability of 81 % was measured (data not shown). In contrast to our results (with particle size of 20 - 40 nm and specific surface area of ~70 m^2 g^{-1}), Labbaf et al. (2011) determined a reduction of hMSC viability to 85 % after being in contact wirth sub-micron sized bioactive glass particles at a concentration of 200 µg ml^{-1}. These sol-gel derived particles exhibit a size in the range of 175 - 250 nm and with a specific surface area of 28 m^2 g^{-1} (Labbaf et al. 2011). Other nanosized biomaterials like TiO_2 influenced also the cell viability. Gerhardt et al. (2007) measured a decrease of MG-63 cell viability of 65 % by the use TiO_2 particles (size 21 nm, specific surface area 50 m²g) with a concentration of 250 µg ml^{-1} after 24 h. Beside the material composition, the size of the particles clearly influences cell - biomaterial - interaction. The size effect was shown by Shi et al. (2009), comparing hydroxyapatite particles in the range of 20, 80 and 500 nm. HAp particles of 20 nm size were seen to support cell proliferation and inhibit apoptosis in MG-63 osteoblast-like cells. Our *in vitro* studies suggest also an increase of cell activity caused by the use of nanosized BG compared to the microsized particles. One reason could be that bioactive glass dissolution products have been shown to upregulate a number of genes in several cell types and above all in osteoblasts (Jell and Stevens 2006). Especially, BG degradation products like Si and P can influence ALP. Given the positive results of the present investigation, future work will consider the long term influence of nBG and its dissolution products on osteoblast-like cells and on the differentiation behaviour of precursor cells.

5. Conclusion

Our study represents a novel detailed observation of physico-chemical reactions occurring on nanoscaled bioactive 45S5 (nBG) particles in simulated body fluid (SBF). XRD, FT-IR and TEM investigations revealed a very rapid formation of carbonated nanocrystalline hydroxyapatite after 1d of immersion in SBF. The initial network of agglomerated primary nanoscaled particles was shown to be distorted and the particle size is reduced upon the dissolution process. Furthermore, nBG particles co-precipitation of nanocrystalline and large calcite was observed by TEM after 1 day likely due to the higher surface area and, thus, higher reactivity of the nBG particles in comparison to conventional (μBG) particles. These findings bring new insight in the reactions kinetics of nanoscaled 45S5 bioactive glass particles which are relevant for applications of nBG in tissue engineering and for considerations for in vitro cells test carried out on this material. Furthermore, the *in vitro* investigation with MG-63 osteoblast-like cells revealed a high cytocompatibility of the nBG particles compared to μBG. It seems that particles size and material composition enhanced cell growth and activity. Thus, the nanoscaled 45S5 bioactive glass particles can be considered as well promising material for bone tissue engineering, providing very fast kinetics for bone-like hydroxyapatite mineralisation without any toxic effects on osteoblast cells.

Acknowledgments

We thank Alexandra Grigore (Institute of Biomaterials, University of Erlangen-Nürnberg) for supporting the cell culture experiments. Stefan Romeis, Claudia Eisermann and Nadine Depner from Institute of Particle Technology (University of Erlangen-Nürnberg) are gratefully acknowledged for discussions and experimental assistance. The German Research Society (DFG) is gratefully acknowledged for the financial support. Prof. Ben Fabry is acknowledged for allowing us to carry out experiments in his laboratory.

References

Hench LL, Xynos ID, Polak JM (2004) Bioactive glasses for in situ tissue regeneration. J Biomater Sci Polym Ed 15:543-562.

Gabbi C, Cacchioli A, Locardi B, Guadagnino E (1995) Bioactive glass coating: physicochemical aspects and biological findings. Biomaterials 16(7):515-520.

Rezwan K, Chen QZ, Blaker JJ, Boccaccini AR (2006) Biodegradable and bioactive porous polymer/inorganic composite scaffolds for bone tissue engineering Biomaterials 27(18):3413-3431.

Boccaccini AR, Blaker JJ, Maquet V, Jerome R, Blacher S, Roether JA (2005) Biodegradable and bioactive polymer/Bioglass (R) composite foams for tissue engineering scaffolds. In: Uskokovic DP, Milonjic SK, Rakovic DI (editors) Mater Sci Forum, pp 499-506.

Hench LL (1998) Bioceramics. J Am Ceram Soc 81(7):1705-1728.

Kokubo T, Ito S, Huang ZT, Hayashi T, Sakka S, Kitsugi T, Yamamuro T (1990) Ca, P-rich layer formed on high-strength bioactive glass-ceramic A-W. J Biomed Mater Res 24(3):331-343.

Kokubo T. Bioactive glass ceramics: properties and applications (1991) Biomaterials 12(2):155-163.

Bohner M, Lemaitre J (2009) Can bioactivity be tested in vitro with SBF solution? Biomaterials 30(12):2175-2179.

Kokubo T, Takadama H (2006) How useful is SBF in predicting in vivo bone bioactivity? Biomaterials 27(15):2907-2915.

Ohtsuki C, Aoki Y, Kokubo T, Bando Y, Neo M, Nakamura T (1995) Transmission electron-microscopic observation of glass-ceramic A-W and apatite layer formed on its surface in a simulated body-fluid. J Ceram Soc Jpn 103(5):449-454.

Brunner TJ, Grass RN, Stark WJ (2006) Glass and bioglass nanopowders by flame synthesis. Chem Commun 13:1384-1386.

Boccaccini AR, Erol M, Stark WJ, Mohn D, Hong Z, Mano JF (2010) Polymer/bioactive glass nanocomposites for biomedical applications: A review. Composites Science and Technology 70(13):1764-1776.

Loher S (2006) Improved degradation and bioactivity of amorphous aerosol derived tricalcium phosphate nanoparticles in poly(lactide-co-glycolide). Nanotechnology 17(8):2054.

Misra SK, Mohn D, Brunner TJ et al (2008) Comparison of nanoscale and microscale bioactive glass on the properties of P(3HB)/Bioglass composites. Biomaterials 29(12):1750-1761.

Lin S, Van den Bergh W, Baker S, Jones JR (2011) Protein interactions with nanoporous sol–gel derived bioactive glasses. Acta Biomater 7(10):3606-3615.

Waltimo T, Brunner TJ, Vollenweider M, Stark WJ, Zehnder M (2007) Antimicrobial effect of nanometric bioactive glass 45S5. J Dent Res 86(8):754-757.

Vollenweider M, Brunner TJ, Knecht S, Grass RN, Zehnder M, Imfeld T, Stark WJ (2007) Remineralization of human dentin using ultrafine bioactive glass particles. Acta Biomater 3(6):936-943.

Curtis AR, West NX, Su B (2010) Synthesis of nanobioglass and formation of apatite rods to occlude exposed dentine tubules and eliminate hypersensitivity. Acta Biomater 6(9):3740-3746.

Nel AE, Madler L, Velegol D et al (2009) Understanding biophysicochemical interactions at the nano-bio interface. Nat Mater 8(7):543-557.

Labbaf S, Tsigkou O, Müller KH, Stevens MM, Porter AE, Jones JR (2011) Spherical bioactive glass particles and their interaction with human mesenchymal stem cells in vitro. Biomaterials 32(4):1010-1018.

Limbach LK, Li Y, Grass RN et al (2005) Oxide Nanoparticle Uptake in Human Lung Fibroblasts: Effects of Particle Size, Agglomeration, and Diffusion at Low Concentrations. Environ Sci Technol 39(23):9370-9376.

Sahay G, Alakhova DY, Kabanov AV (2010) Endocytosis of nanomedicines. J Control Release 145(3):182-195.

Cerruti M, Greenspan D, Powers K (2005) Effect of pH and ionic strength on the reactivity of Bioglass® 45S5. Biomaterials 26(14):1665-1674.

Bunker BC, Tallant DR, Headley TJ et al (1998) Structure of leached sodium borosilicate glass. Phys Chem Glasses 29(3):106-120.

Du H, Williams CT, Ebner AD, Ritter JA (2010) In Situ FTIR Spectroscopic Analysis of Carbonate Transformations during Adsorption and Desorption of CO2 in K-Promoted HTlc. Chem Mater 22(11):3519-3526.

Koutsopoulos S (2002) Synthesis and characterization of hydroxyapatite crystals: A review study on the analytical methods. J Biomed Mater Res 62(4):600-612.

Bosch RF, Adelantado JVG, Moya Moreno MCM (2002) FTIR quantitative analysis of calcium carbonate (calcite) and silica (quartz) mixtures using the constant ratio method. Application to geological samples. Talanta 58(4):811-821.

Danilchenko SN, Kukharenko OG, Moseke C, Protsenko IY, Sukhodub LF, Sulkio-Cleff B (2002) Determination of the Bone Mineral Crystallite Size and Lattice Strain from Diffraction Line Broadening. Cryst Res Technol 37(11):1234-1240.

Cerruti M, Morterra C (2004) Carbonate Formation on Bioactive Glasses. Langmuir 20(15):6382-6388.

Cerruti M, Bianchi CL, Bonino F, Damin A, Perardi A, Morterra C (2005) Surface Modifications of Bioglass Immersed in TRIS-Buffered Solution. A Multitechnical Spectroscopic Study. J Phys Chem B 109(30):14496-14505.

Hench LL (1991) Bioceramics: From concept to clinic. J Am Ceram Soc 74(7):1487-1510.

Jones JR, Sepulveda P, Hench LL (2001) Dose-dependent behavior of bioactive glass dissolution. J Biomed Mater Res 58(6):720-726.

Dey A, Bomans PHH, Müller FA, Will J, Frederik PM, de With G, Sommerdijk NAJM (2010) The role of prenucleation clusters in surface-induced calcium phosphate crystallization. Nat Mater 9(12):1010-1014.

Zhu PX, Masuda Y, Yonezawa T, Koumoto K (2003) Investigation of apatite deposition onto charged surfaces in aqueous solutions using a quartz-crystal microbalance. J Am Ceram Soc 86(5):782-790.

Müller L, Müller FA (2006) Preparation of SBF with different content and its influence on the composition of biomimetic apatites. Acta Biomater 2(2):181-189.

Nielsen AE (1984) Electrolyte crystal growth mechanisms. J Cryst Growth 67(2):289-310.

Davies CW, Shedlovsky T (1964) Ion Association. J Electrochem Soc 111(3):85C-86C.

Elliott JC (1994) Structure and Chemistry of the Apatites and Other Calcium Orthophosphates. Elsevier, Amsterdam.

Antonakos A, Liarokapis E, Leventouri T (2007) Micro-Raman and FTIR studies of synthetic and natural apatites. Biomaterials 28(19):3043-3054.

Pasteris JD, Wopenka B, Freeman JJ et al (2004) Lack of OH in nanocrystalline apatite as a function of degree of atomic order: implications for bone and biomaterials. Biomaterials 25(2):229-238.

Tilocca A (2011) Molecular dynamics simulations of a bioactive glass nanoparticle. J Mater Chem 21(34):12660-12667.

Oyane A, Onuma K, Ito A, Kim HM, Kokubo T, Nakamura T (2003) Formation and growth of clusters in conventional and new kinds of simulated body fluids. J Biomed Mater Res, Part A 64A(2):339-348.

Mozafari M, Moztarzadeh F, Tahriri M (2010) Investigation of the physico-chemical reactivity of a mesoporous bioactive SiO(2)-CaO-P(2)O(5) glass in simulated body fluid. J Non-Cryst Solids 356(28-30):1470-1478.

Pichon BP, Bomans PHH, Frederik PM, Sommerdijk NAJM (2008) A Quasi-Time-Resolved CryoTEM Study of the Nucleation of CaCO3 under Langmuir Monolayers. J Am Chem Soc 130(12):4034-4040.

Sepulveda P, Jones JR, Hench LL (2002) In vitro dissolution of melt-derived 45S5 and sol-gel derived 58S bioactive glasses. J Biomed Mater Res 61(2):301-311.

Heng B, Zhao X, Xiong S, Ng K, Boey F, Loo J (2011) Cytotoxicity of zinc oxide (ZnO) nanoparticles is influenced by cell density and culture format. Arch Toxicol 85(6):695-704.

Gann H, Glaspell G, Garrad R et al (2010) Interaction of MnO and ZnO Nanomaterials with Biomedically Important Proteins and Cells. J Biomed Nanotechnol 6(1):37-42.

Gerhardt LC, Jell GMR, Boccaccini AR (2007) Titanium dioxide (TiO2) nanoparticles filled poly(D,L lactid acid) (PDLLA) matrix composites for bone tissue engineering. Journal of Materials Science-Materials in Medicine 18(7):1287-1298.

Shi Z, Huang X, Cai Y, Tang R, Yang D (2009) Size effect of hydroxyapatite nanoparticles on proliferation and apoptosis of osteoblast-like cells. Acta Biomater 5(1):338-345.

Jell G, Stevens M (2006) Gene activation by bioactive glasses. J Mater Sci: Mater Med 17(11):997-1002.

Elliott JC, Mackie PE, Young RA (1973) Monoclinic Hydroxyapatite. Science 180(4090):1055-1057.

Ito A, Maekawa K, Tsutsumi S, Ikazaki F, Tateishi T (1997) Solubility product of OH-carbonated hydroxyapatite. J Biomed Mater Res 36(4):522-528.

Tang R, Henneman ZJ, Nancollas GH (2003) Constant composition kinetics study of carbonated apatite dissolution. J Cryst Growth 249(3-4):614-624.

Berner RA (1976) The solubility of calcite and aragonite in seawater at atmospheric pressure and 34.5 0 / 00 salinity. Am J Sci 276(6):713-730.

Figure captions:

Table 1: Properties of the materials used in the study.

Table 2: Chemical composition of the melt-derived and flame synthesized bioactive 45S5 glass (in wt.%.).

Table 3: Ion concentrations of the simulated body fluid (SBF) and human blood plasma (Boccaccini et al. 2010).

Table 4: Overview over the main peaks detected in the FT-IR spectra of nBG and µBG prior and after soaking in SBF for different time points.

Table 5: Ionic product and degree of supersaturation calculated for hydroxyapatite and calcite.

Fig. 1: FTIR spectra of a) nanosized 45S5 bioactive glass particles (nBG) and b) micron-sized 45S5 bioactive (µBG) glass particles: as-prepared and after immersion in SBF for 4h, 8h, 24h, 3d and 7 d, respectively.

Fig. 2: XRD spectra of a) nanosized 45S5 bioactive glass (nBG) and b) micron-sized 45S5 bioactive glass (µBG) after immersion in SBF for 1d, 3d and 7d.

Fig. 3: TEM images and selected area electron diffraction (SAED) patterns of nBG particles: a) and b) as-prepared, c) - f) after immersion for 1 day in SBF solution. After 1 day immersion in SBF the formation of nanocrystalline and large calcite precipitates and nanocrystalline HA is observed.

Fig. 4: TEM images and selected area electron diffraction (SAED) patterns of nBG after immersion for 7 days in SBF: a) – d) nanocrystalline and large calcite precipitates, coexisting with unreacted nBG; e) and f) compact agglomerates composed of HA and unreacted nBG.

Fig. 5: LDH-activity of MG-63 cell cultured on µBG, nBG and ZnO in the range of 0-200 µg ml^{-1} over 48 h (normalized in each case to 0 µg ml^{-1} = 100 %, * $p < 0.05$).

Fig. 6: Mitochondrial activity MG-63 cell cultured on µBG, nBG and ZnO in the range of 0-200 µg ml^{-1} over 48 h (normalized in each case to 0 µgml^{-1} = 100 %, * $p < 0.05$).

Fig. 7: LM-images of MG-63 cultured on a) ZnO particles b) on µBG particles and c) nBG particles in the range of 0-200 µg ml^{-1} for 48 h.

Fig. 8: CLM-images of MG-63 cultured on 0 (left) 200 µg ml^{-1} µBG (centre) and 200 µg ml^{-1} nBG (right) particles in the range of 0-200 µg ml^{-1} for 48 h.

Fig. 9: Specific ALP-Activity of MG-63 cell cultured on µBG and nBG in the range of 0-200 µg ml^{-1} over 48 h (normalized in each case to 0 µg ml^{-1} = 100 %, * $p < 0.05$).

Fig. 10: Proposed model for HAp formation and co-precipitation of calcite on nanoscaled bioactive glass powder during immersion in SBF.

Table 1

Material	Sample code	Particle size	Specific surface (m^2g^{-1})
Melt-derived 45S5 glass	µBG	10 µm	1-2
Flame-synthesized 45S5 glass	nBG	20-60 nm	60-80
Zinc oxide	ZnO	0.5-1.5 µm	6.5

Table 2

	SiO_2	CaO	Na_2O	P_2O_5
nBG	47.8	25.1	22.6	4.6
µBG	44.97	24.55	24.55	5.99

Table 3

Ion	Na^+	K^+	Mg^{2+}	Ca^{2+}	Cl^-	HCO^{3-}	HPO_4^{2-}	SO_4^{2-}
Blood plasma	142	3,6-5,5	1	2,12	95-107	27	0,6-1,4	0.5
SBF	142	5,0	1,5	2,5	148,8	4,2	1,0	0.5

Table 4

Assignment	Position (cm^{-1}) and shape	Time point of appearance*		Remarks	Reference
		nBG	µBG		
ν_{sym}(Si-O-Si)	~490-500 ~450	as-prepared state all stages of reaction in SBF		Shifted to 450 due to leaching of cations; ν_{sym}(Si-O-Si) at ~450 $cm^{-1}$is also observed for pure silica.	(Cerruti et al. 2005) (Bunker et al. 1998)
P-O band	Broad band at ~560-610	4h	1d	Characteristic band for amorphous calcium phosphate.	(Cerruti et al. 2005)
ν_4(P-O-P)	Sharp double peak at ~570 and ~600	1d	3d	Bending mode of P-O-P bond found in hydroxyapatite.	(Koutsopoulos 2002)
CO_3^{2-}	Small peak at ~712	3d	not visible	Characteristic band for calcite.	(Du et al. 2010)
δ(Si-O-Si)	Peak at ~800	4h	3d	3D silica structures	(Cerruti et al. 2005)
$\nu_2(CO_3^2)$	Sharp peak at ~871	permanent	3d	Characteristic band for CO_3^{2-}group in carbonated apatites. For nBG this band is related to both carbonates adsorbed on the surface and CO_3^{2-} substituted in the apatite layer. See discussion.	(Koutsopoulos 2002)
SiO_{NBO}	Shoulder at ~930	as-prepared state		The SiO_{NBO} is decreasing in intensity due to cation leaching.	(Cerruti et al. 2005; Bunker et al. 1998)
ν_{asym}(Si-O-Si)	Intense broad band at ~1020	as-prepared state		The broad complex band at 900-1200 is difficult to analyse due to overlapping as both PO and SiO groups absorb in this region.	(Cerruti et al. 2005;Koutsopoulos 2002)
(Si-O-Si) bonds	Shoulder at ~1210	all stages of reaction in SBF		Formation of new Si-O-Si bonds upon condensation of SiOH groups. Appearance of this band corresponds to the decrease of the SiO_{NBO} peak.	(Cerruti et al. 2005; Jones et al. 2001)
$\nu_3(CO_3^{2-})$	Broad peak at ~1460	as-prepared state		Observed for symmetrically coordinated pure ionic carbonate ions adsorbed on surfaces. The intensity of the peak is higher for nBG compared to µBG.	(Du et al. 2010; Cerruti and Morterra 2004)
	Double peak at ~1430 and ~1500	all stages of reaction in SBF		These bands can be attributed either to Ca^{2+} coordinated CO_3^{2-} adsorption [29-30] or carbonate ions substituted in carbonated apatites [26]. Please note: for µBG a sharp increase in intensity of this double peak after 3 d is attended by the appearance of the $\nu_2(CO_3^2)$ band at ~871 cm^{-1}.	
δ(H_2O)	Small peak at ~1630	all stages of reaction in SBF		Coordinated water molecules adsorbed on the surface.	(Cerruti et al. 2005)

***related to immersion in SBF**

Table 5

Phase	Formula	*-log(IP)*	*S*
Stoichiometric hydroxyapatite, sHA	$Ca_{10}(PO_4)_6(OH)_2$)	97.6	1.1
Type-A carbonated hydroxyapatite, A-CHA	$Ca_{10}(PO_4)_6(CO_3)_{0,5}(OH)$	93.0	19.6
Type B carbonated hydroxyapatite, B-CHA	$Ca_9(HPO_4)_6(PO_4)_5(CO_3)_{0,5}(OH)$	90.8	19,8
Calcite	$CaCO_3$	22.8	$8 \cdot 10^{-8} \cong 0$

***IP*=Ionic activity; *S*=Saturation of the SBF in respect to corresponding phase. *Ksp* values for HA, A-CHA, B-CHA and calcite were taken from Elliot et al. (1973), Ito et al. (1997), Tang et al. (2003), and Berner 1976, respectively.**

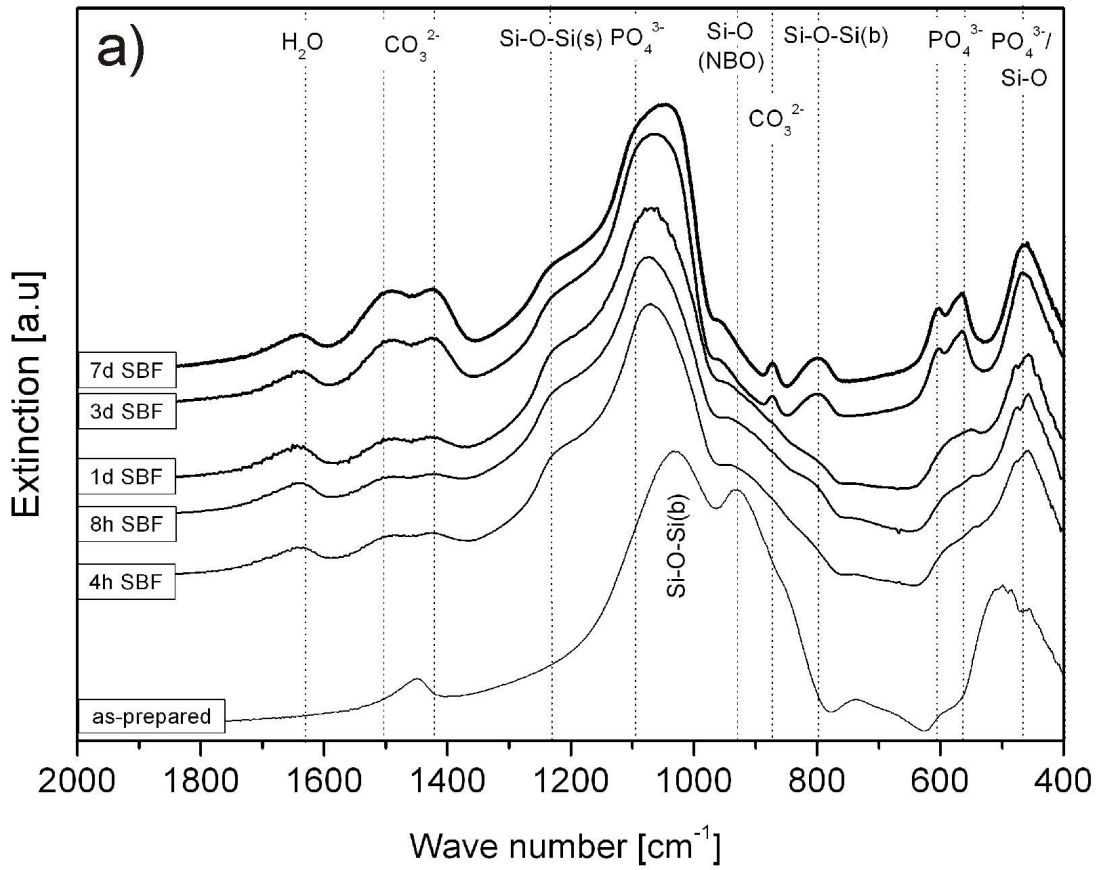
a)
H2O
CO3 2-
Si-O-Si(s)
PO4 3-
Si-O (NBO)
Si-O-Si(b)
PO4 3-
PO4 3-/ Si-O
CO3 2-
7d SBF
3d SBF
1d SBF
8h SBF
4h SBF
as-prepared
Si-O-Si(b)
Extinction [a.u]
2000
1800
1600
1400
1200
1000
800
600
400
Wave number [cm-1]

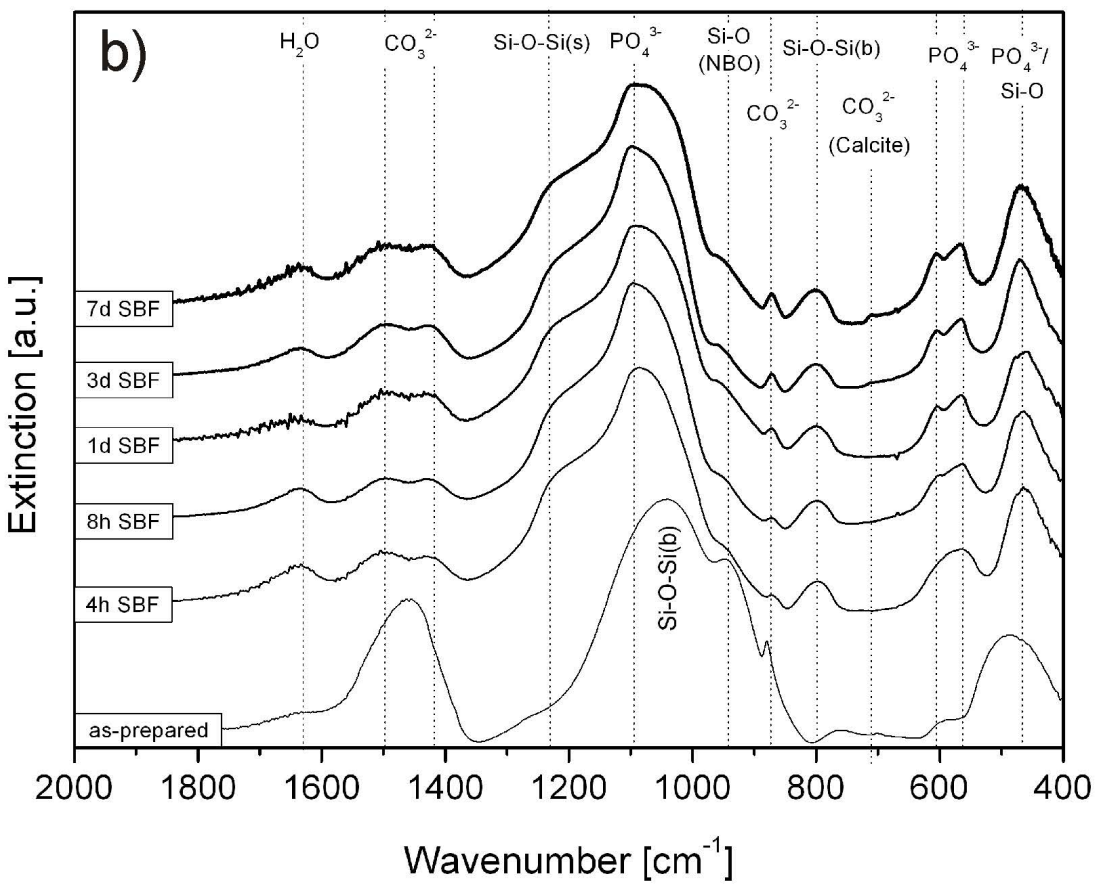
b)
H2O
CO3 2-
Si-O-Si(s)
PO4 3-
Si-O (NBO)
Si-O-Si(b)
PO4 3-
PO4 3-/ Si-O
CO3 2-
CO3 2- (Calcite)
7d SBF
3d SBF
1d SBF
8h SBF
4h SBF
as-prepared
Si-O-Si(b)
Extinction [a.u.]
2000
1800
1600
1400
1200
1000
800
600
400
Wavenumber [cm-1]

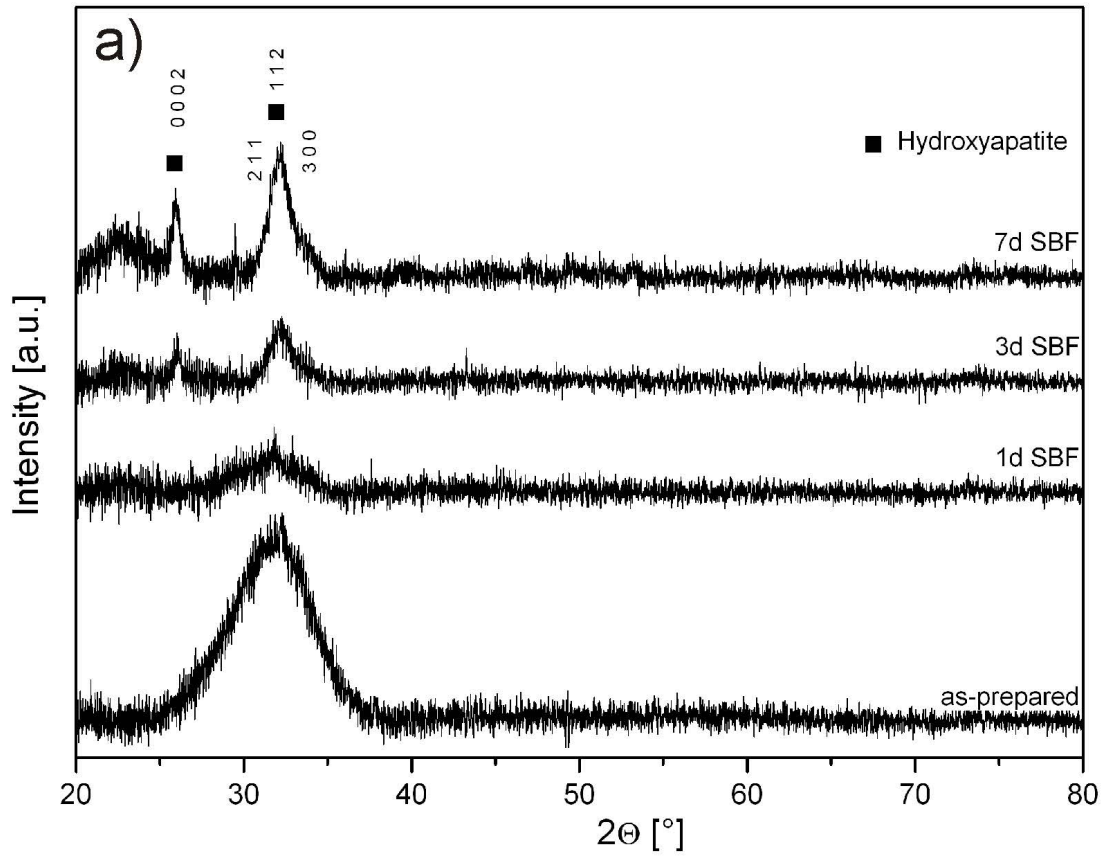
a)
0002
112
211
300
Hydroxyapatite
7d SBF
3d SBF
1d SBF
as-prepared
Intensity [a.u.]
20
30
40
50
60
70
80
2Θ [°]

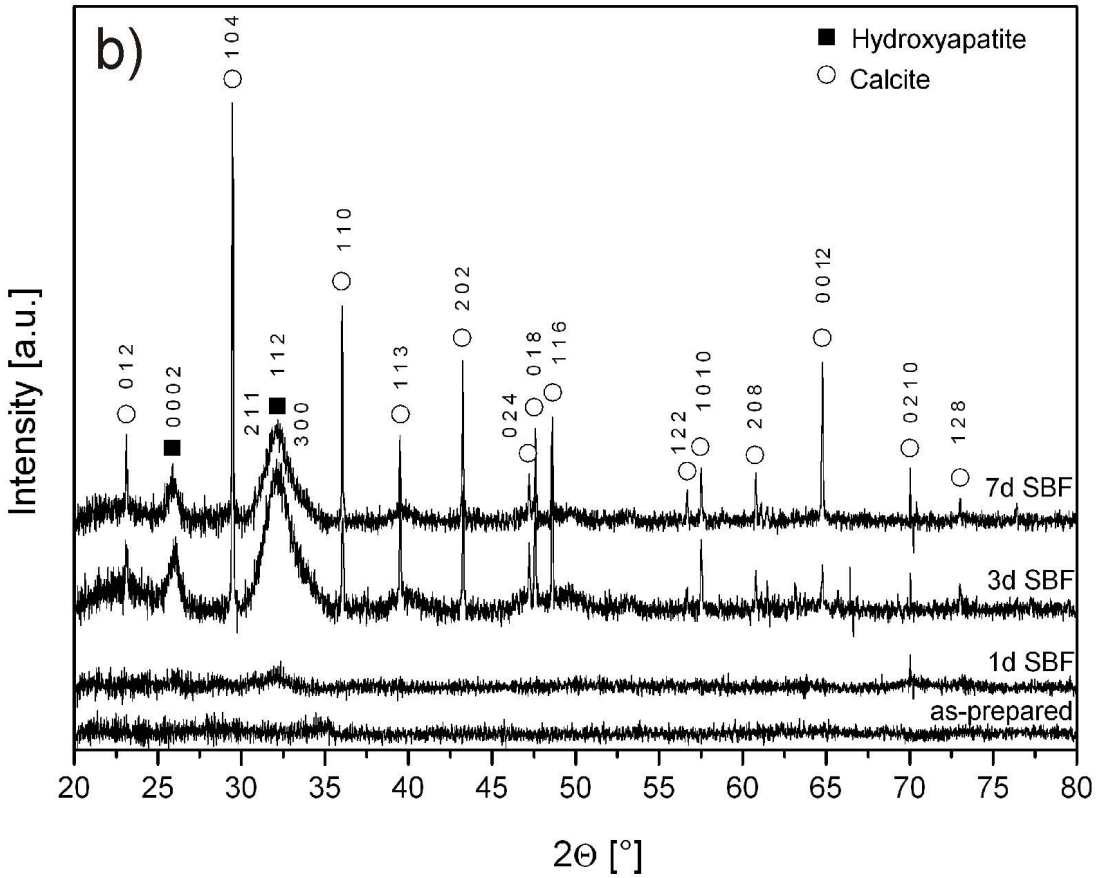
b)
Hydroxyapatite
Calcite
104
012
0002
211
112
300
110
113
202
024
018
116
122
1010
208
0012
0210
128
7d SBF
3d SBF
1d SBF
as-prepared
Intensity [a.u.]
20
25
30
35
40
45
50
55
60
65
70
75
80
2Θ [°]

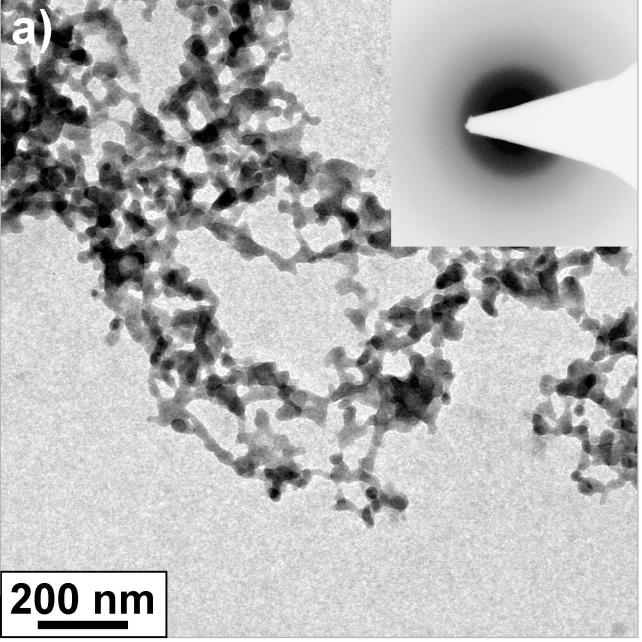
a)
200 nm

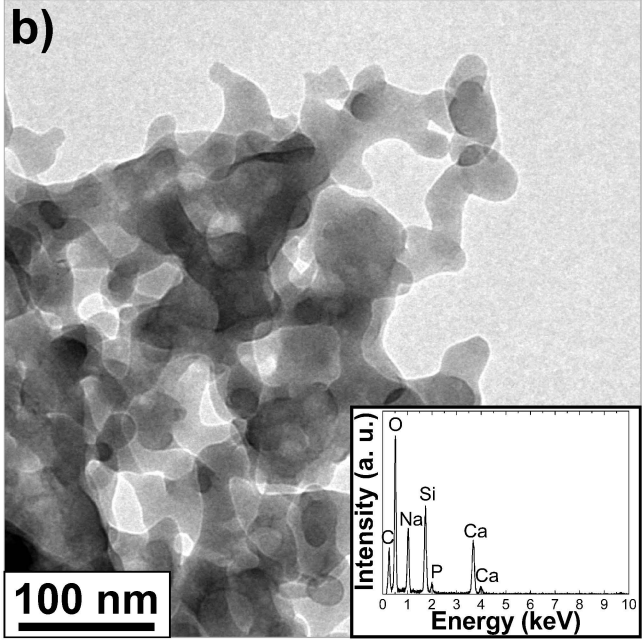
b)
100 nm
Intensity (a. u.)
O
Si
Na
C
Ca
P
Ca
0 1 2 3 4 5 6 7 8 9 10
Energy (keV)

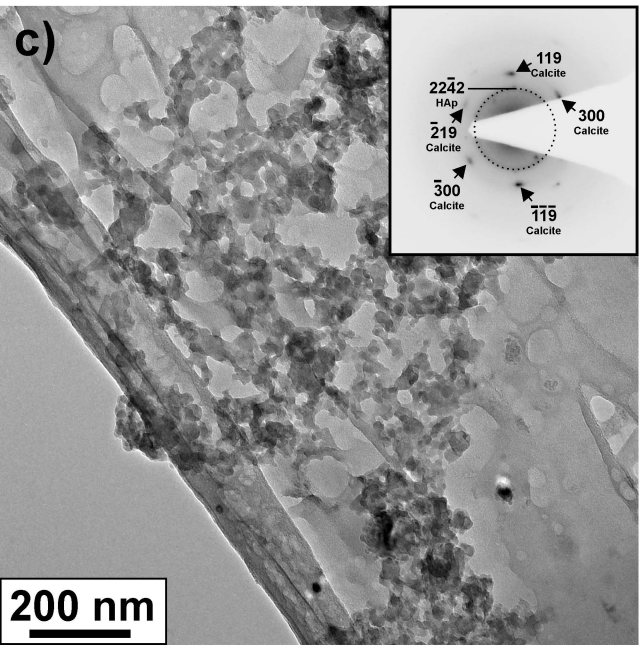
c)
200 nm
119
Calcite
22$\bar{4}$2
HAp
300
Calcite
$\bar{2}$19
Calcite
$\bar{3}$00
Calcite
$\bar{1}\bar{1}\bar{9}$
Calcite

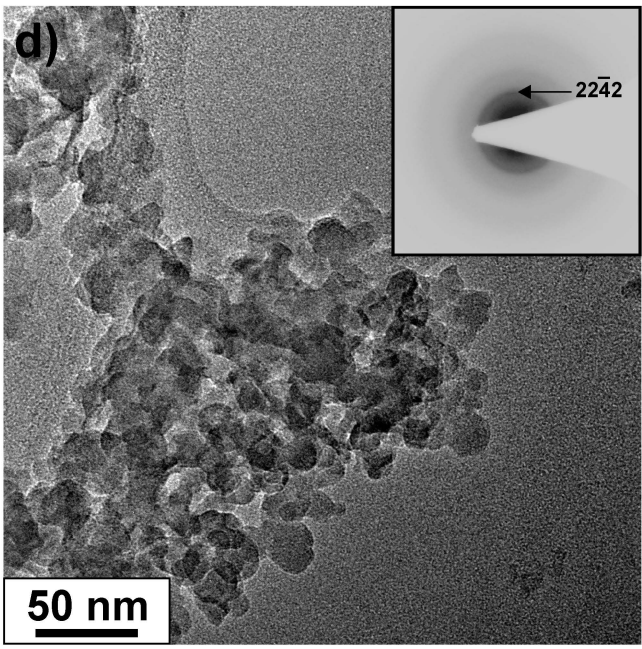
d)
50 nm
22$\bar{4}$2

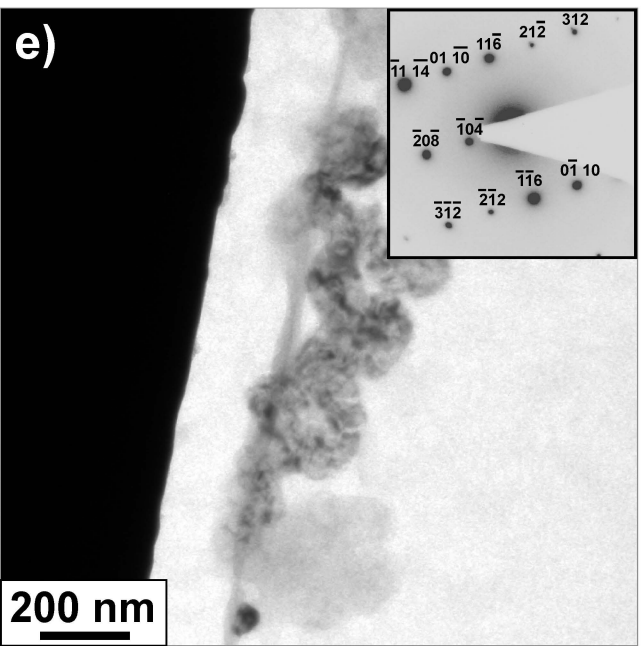
e)
200 nm
$\bar{1}$1 1$\bar{4}$
01 $\bar{1}$0
11$\bar{6}$
21$\bar{2}$
312
$\bar{2}$08
$\bar{1}$04
$\bar{1}$16
01 $\bar{1}$0
$\bar{3}\bar{1}\bar{2}$
$\bar{2}\bar{1}\bar{2}$

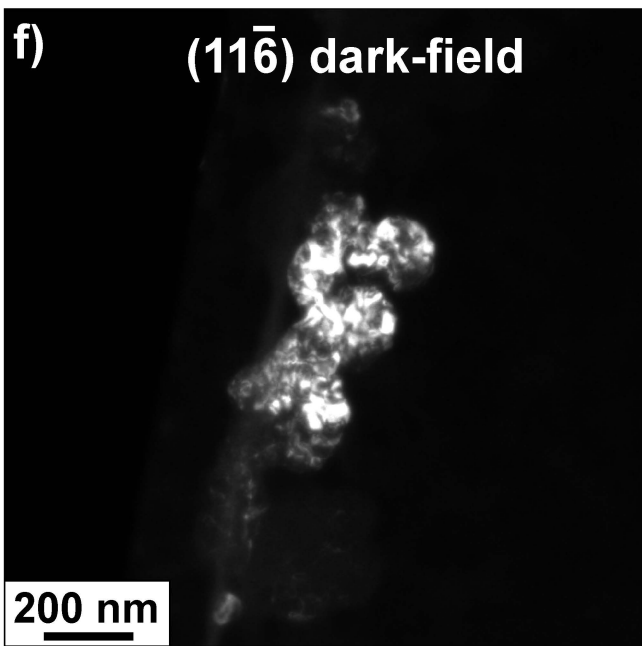
f)
(11$\bar{6}$) dark-field
200 nm

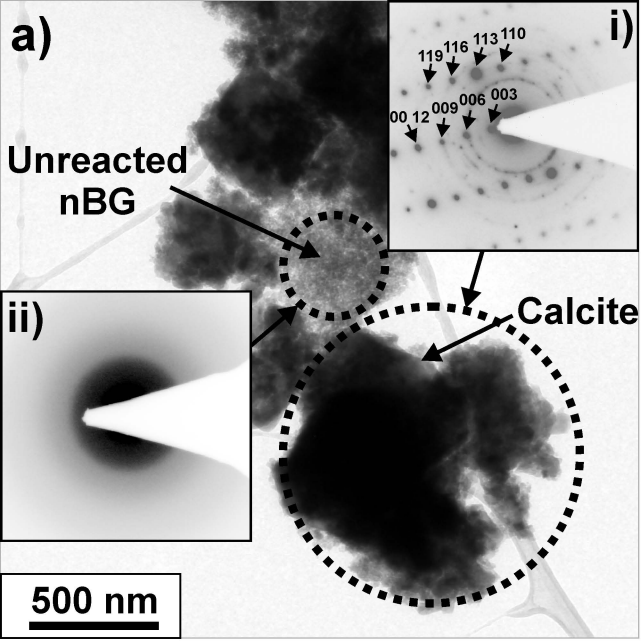
a)
i)
119
116
113
110
00 12
009
006
003
Unreacted
nBG
ii)
Calcite
500 nm

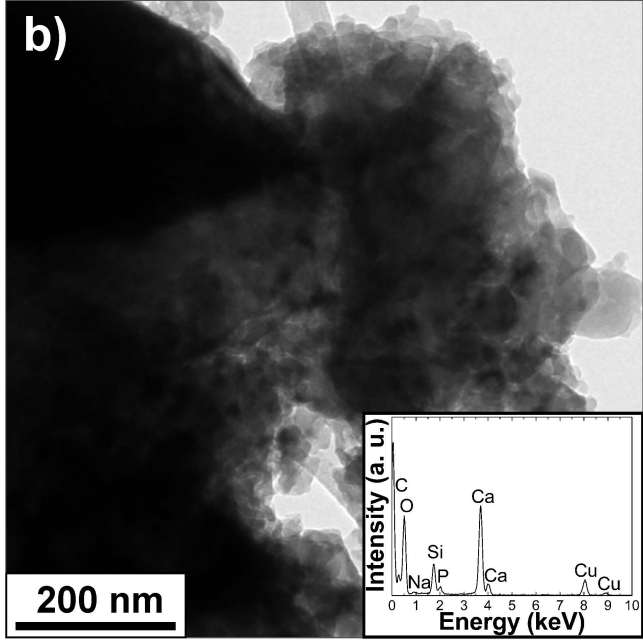
b)
Intensity (a. u.)
C
O
Ca
Si
Na
P
Ca
Cu
Cu
0 1 2 3 4 5 6 7 8 9 10
Energy (keV)
200 nm

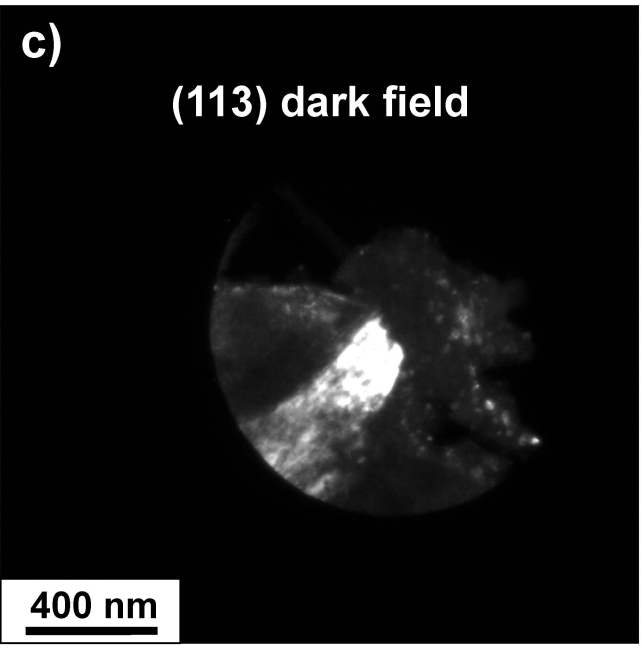
c)
(113) dark field
400 nm

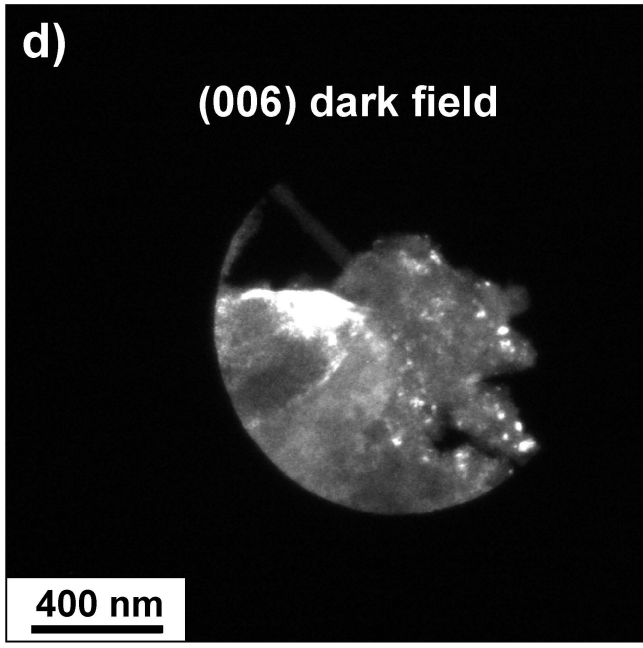
d)
(006) dark field
400 nm

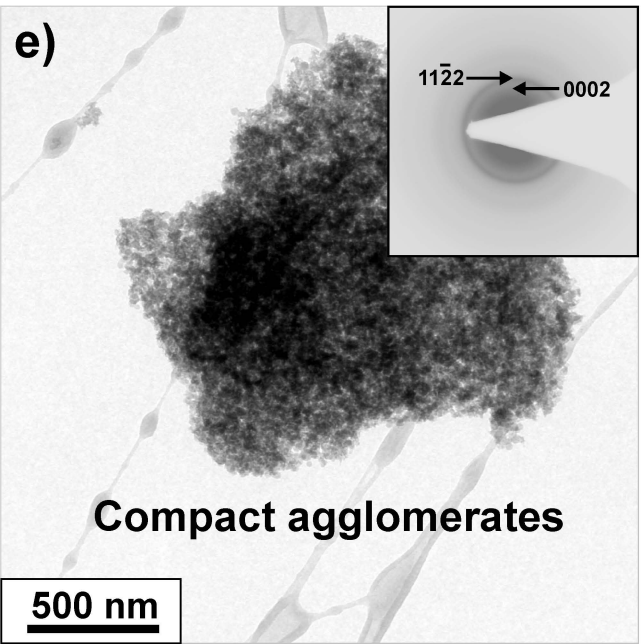
e)
11$\bar{2}$2
0002
Compact agglomerates
500 nm

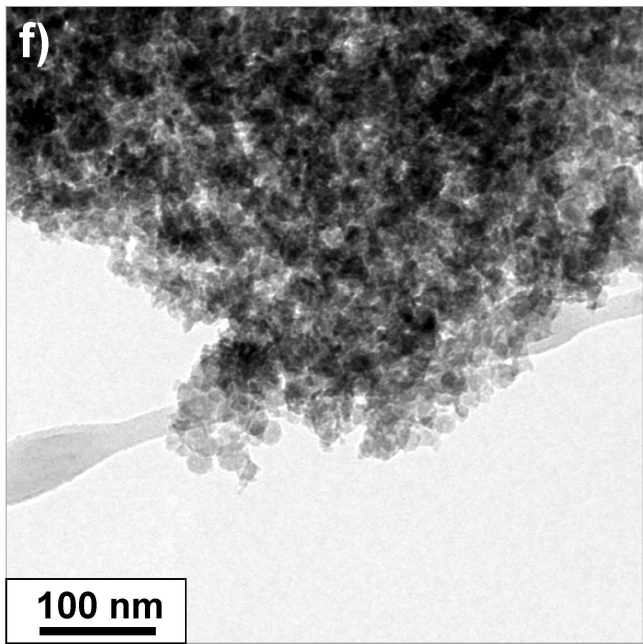
f)
100 nm

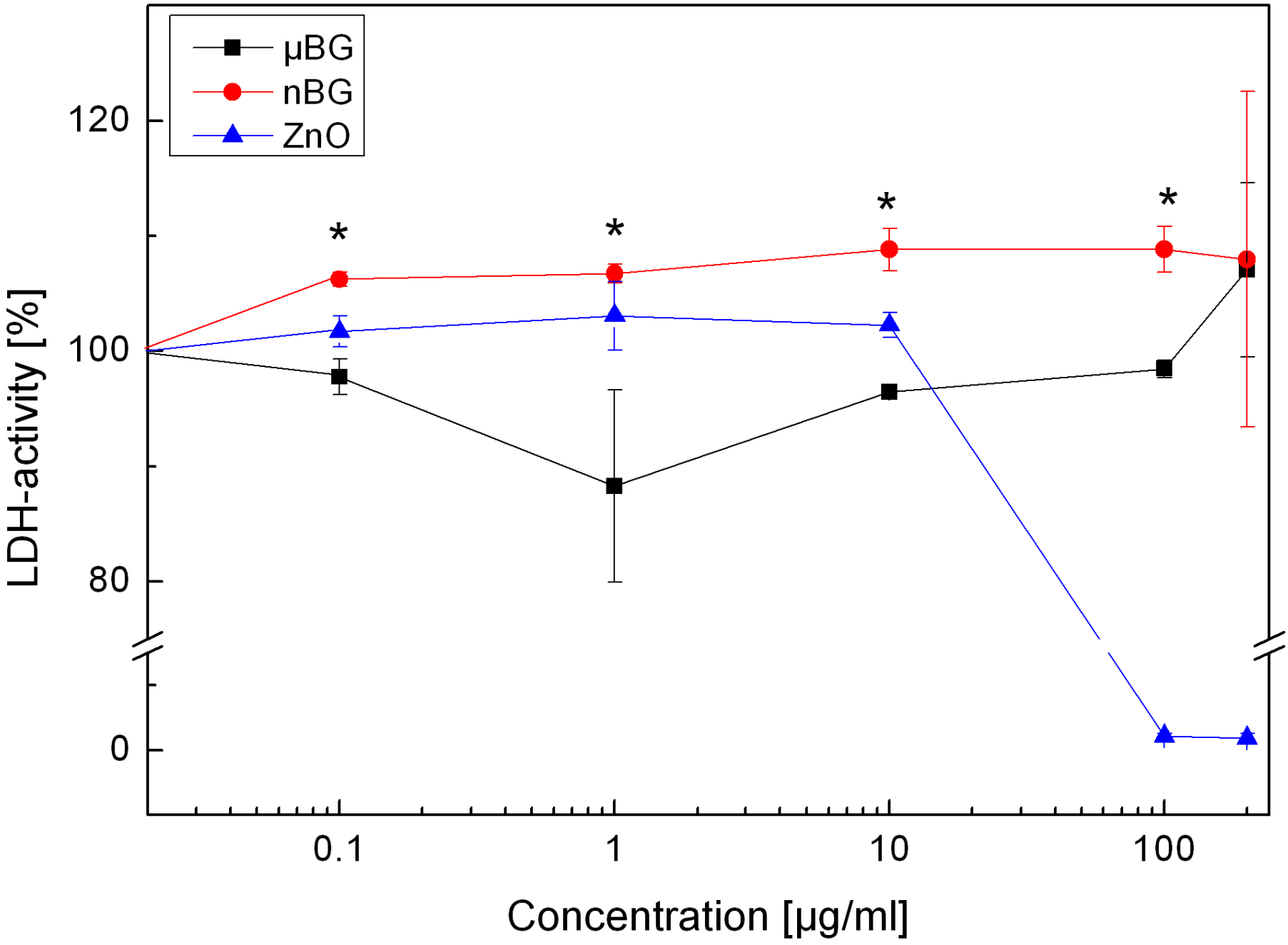
μBG
nBG
ZnO
LDH-activity [%]
120
100
80
0
*
*
*
*
0.1
1
10
100
Concentration [μg/ml]

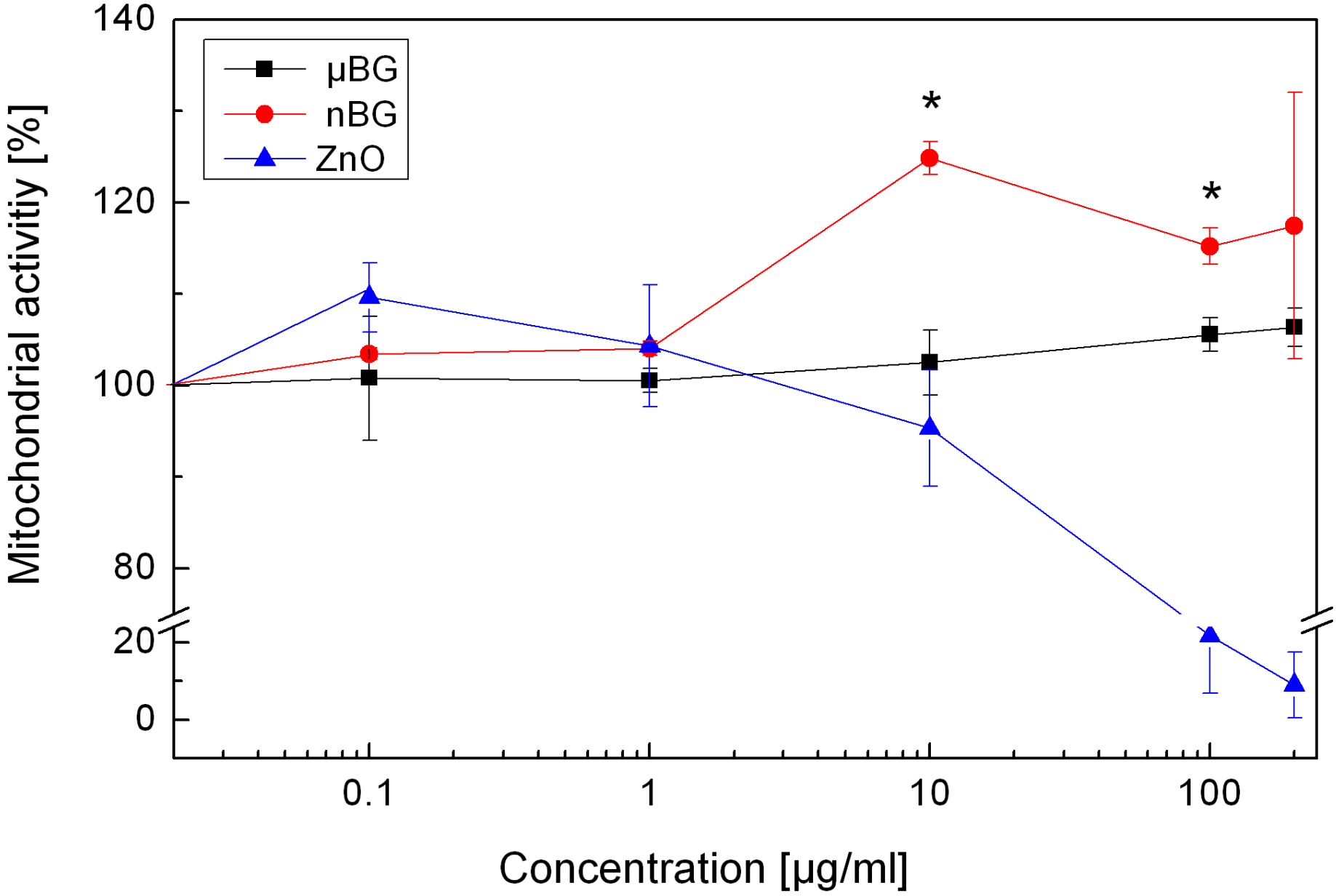
140
120
100
80
20
0
Mitochondrial activitiy [%]
μBG
nBG
ZnO
*
*
0.1
1
10
100
Concentration [μg/ml]

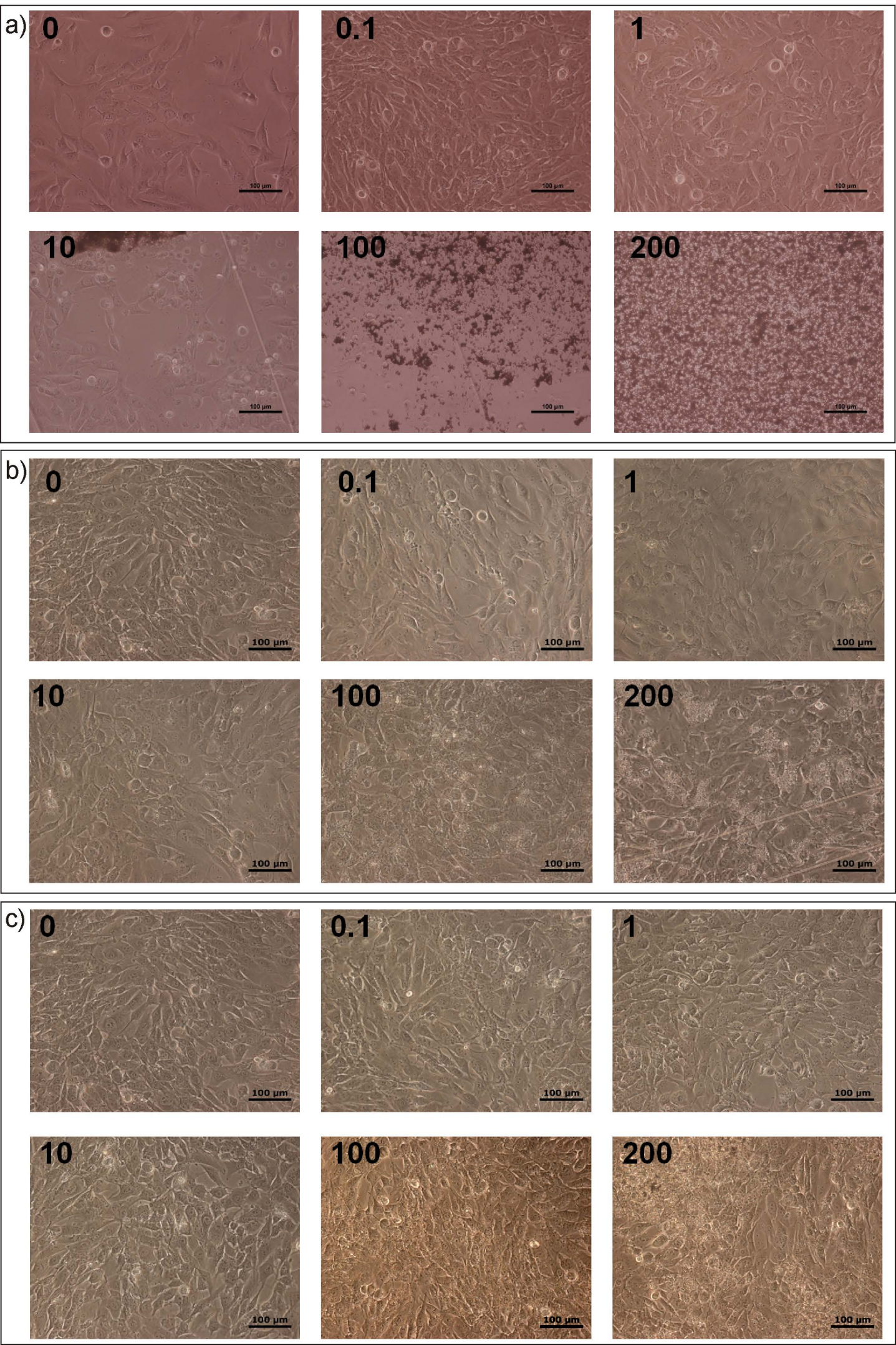
a)
0
0.1
1
10
100
200
100 µm
b)
0
0.1
1
10
100
200
100 µm
c)
0
0.1
1
10
100
200
100 µm

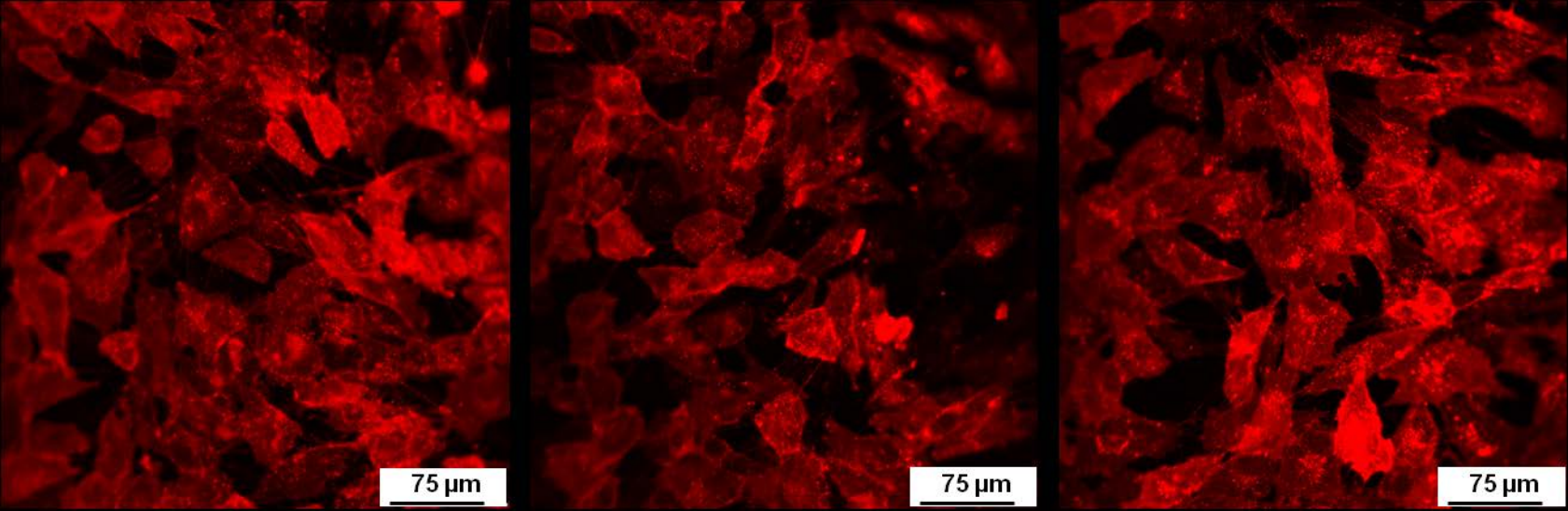
75 µm
75 µm
75 µm

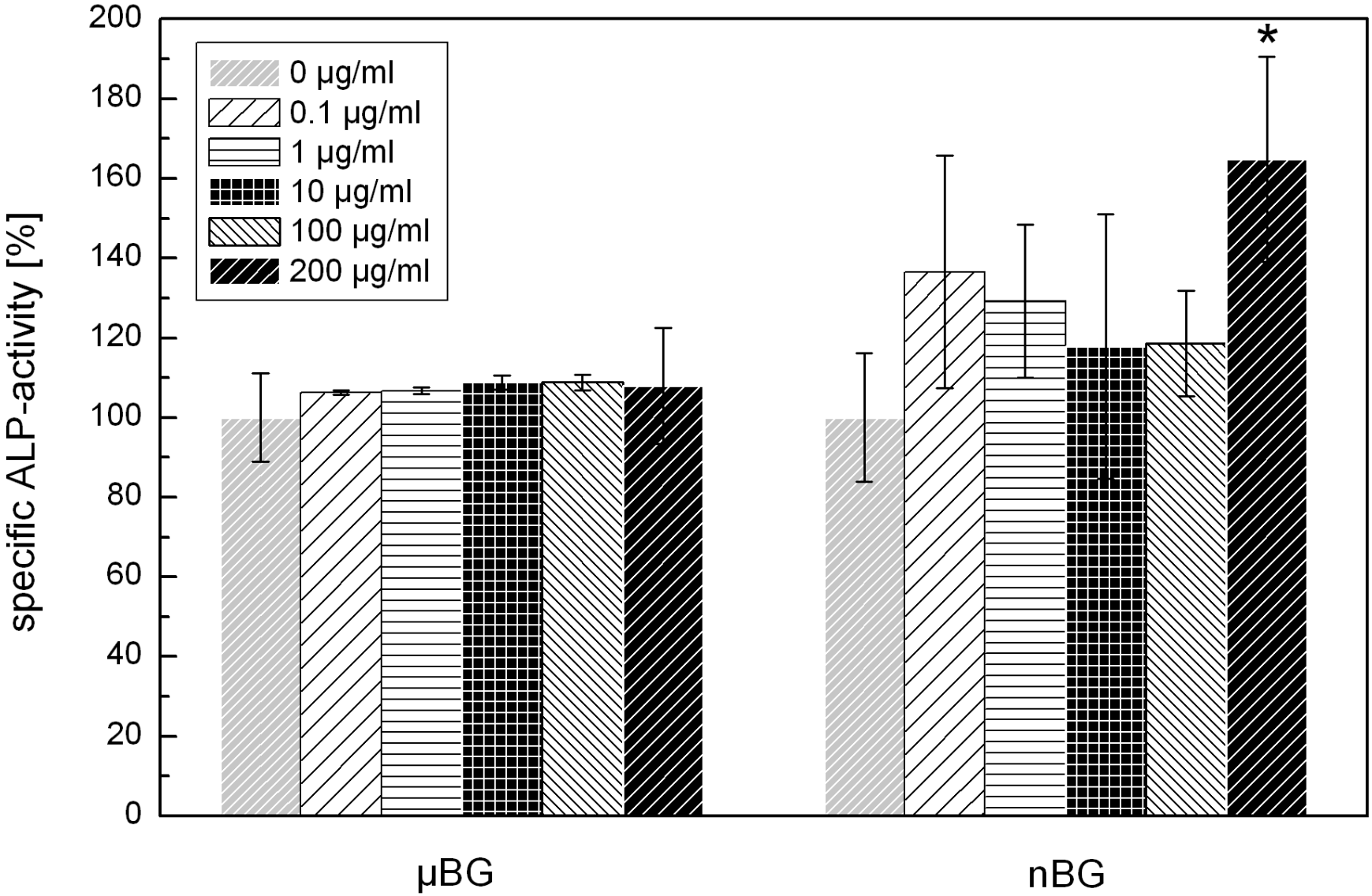
specific ALP-activity [%]
200
180
160
140
120
100
80
60
40
20
0
0 µg/ml
0.1 µg/ml
1 µg/ml
10 µg/ml
100 µg/ml
200 µg/ml
*
µBG
nBG

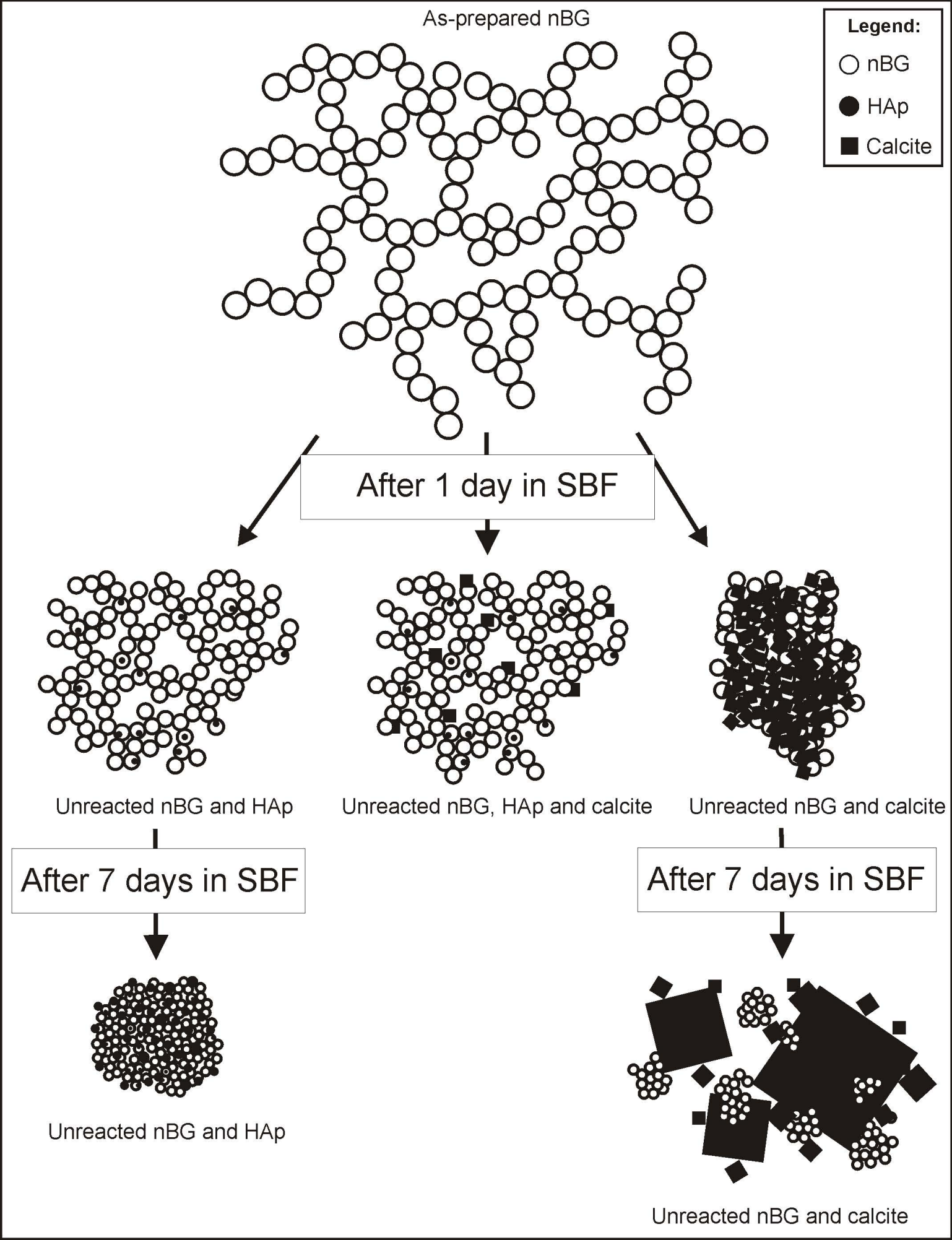
As-prepared nBG
Legend:
nBG
HAp
Calcite
After 1 day in SBF
Unreacted nBG and HAp
Unreacted nBG, HAp and calcite
Unreacted nBG and calcite
After 7 days in SBF
After 7 days in SBF
Unreacted nBG and HAp
Unreacted nBG and calcite